Rational Designing of Bimetallic/Trimetallic HER Catalysts through Supervised Machine Learning

M.Sc. Thesis

By

NEERAJ KUMAR PANDIT

DEPARTMENT OF CHEMISTRY

INDIAN INSTITUTE OF TECHNOLOGY INDORE

MAY 2022

Rational Designing of Bimetallic/Trimetallic HER Catalysts through Supervised Machine Learning

A THESIS

Submitted in partial fulfillment of the
requirements for the award of the degree
of
MASTER OF SCIENCE

by
NEERAJ KUMAR PANDIT

DEPARTMENT OF CHEMISTRY
INDIAN INSTITUTE OF TECHNOLOGY INDORE
MAY 2022

INDIAN INSTITUTE OF TECHNOLOGY INDORE

CANDIDATE'S DECLARATION

I hereby certify that the work which is being presented in the thesis entitled **Rational Designing of Bimetallic/Trimetallic HER Catalysts through Supervised Machine Learning** in the partial fulfillment of the requirements for the award of the degree of **MASTER OF SCIENCE** and submitted in the **DEPARTMENT OF CHEMISTRY, Indian Institute of Technology Indore**, is an authentic record of my own work carried out during the time period from July 2021 to May 2022 under the supervision of Prof. Biswarup Pathak, Professor, Department of Chemistry, Indian Institute of Technology Indore.

The matter presented in this thesis has not been submitted by me for the award of any other degree of this or any other institute.

Neeraj 19/05/2022
Signature of the student with date
(Neeraj Kumar Pandit)

This is to certify that the above statement made by the candidate is correct to the best of my knowledge.

19-05-22
Signature of the Supervisor of M.Sc. thesis with date
(Prof. Biswarup Pathak)

Neeraj Kumar Pandit has successfully given his M.Sc. Oral Examination held on **25 May 2022**.

Signature of Supervisor of M.Sc. thesis
Prof. Biswarup Pathak
Date: 26/05/22

Tushar Kanti Mukherjee.
Convener, DPGC
Date: 26/05/2022

Signature of PSPC Member
Prof. Sanjay Kumar Singh
Date: 26.05.2022

Tridib K Sarma 26.05.2022
Signature of PSPC Member
Dr. Tridib Kumar Sarma
Date:

Acknowledgments

With great pleasure, I want to express my deepest gratitude to my thesis supervisor Prof. Biswarup Pathak (Professor, Department of Chemistry, Indian Institute of Technology Indore), for providing me an opportunity to undertake my research project under his research group. His constant guidance, timely support, and motivation have been constructive to complete this M.Sc. project. His enthusiasm and dedication have always inspired me.

My sincere thanks must also go to the PSPC members of my thesis: Prof. Sanjay Kumar Singh and Dr. Tridib Kumar Sarma, for their valuable suggestions and kind support.

I am grateful to Prof. Suhas S. Joshi, present Director, and Prof. Neelesh Kumar Jain, past Director, Indian Institute of Technology Indore, for encouraging and providing the required facilities at the institute.

I would like to acknowledge the Indian Institute of Technology Indore for providing laboratory and computational facilities during my research project.

I am very grateful to Head, Department of Chemistry, Indian Institute of Technology Indore to constantly motivate me to research and providing us a nice environment. I would also like to thank Prof. Rajneesh Misra, Prof. Suman Mukhopadhyay, Prof. Apurba K. Das, Prof. Sampak Samanta, Dr. Anjan Chakraborty, Dr. Tushar Kanti Mukherjee, Dr. Shaikh M. Mobin, Dr. Satya S. Bulusu, Dr. Chelvam Venkatesh, Dr. Amrendra Kumar Singh, Dr. Abhinav Raghuvanshi, Dr. Dipak Kumar Roy, Dr. Selvakumar Sermadurai, and Dr. Umesh A. Kshirsagar for their guidance and help throughout my M.Sc. course. I have benefited significantly from the Chemistry office staff's indeed professional support: Mr. Manish Kushwaha, Mr. Parthiban P. K., Ms. Vinita Kothari, and Mr. Rameshwar Dauhare.

I owe a special thanks to my project mentor Mr. Diptendu Roy for helping and guiding me throughout the project. I am also very fortunate to have such senior lab members Dr. Shyama Charan Mandal, Dr. Akhil S. Nair, Dr. Mohan Tiwari, Mr. Sandeep Das, Mr. Arunendu Das, Mr. Surya Shekhar Manna, Mr. Amitabha Das, Mr. Milan Kumar Jena, Mrs. Nishchal Bharadwaj, Ms. Eti Mahal, Ms. Sneha Mittal, Mr. Souvik Manna, Ms. Harpriya Minhas, and Mr. Rahul Kumar Sharma. I would also like to thank them for the help in every aspect, friendly discussions, lunch breaks, endless treats, and good times outside the lab.

I would personally like to extend my admiration to all my batchmates during my complete M.Sc. journey.

Most importantly, I sincerely thank my parents (Mr. Anil Pandit and Mrs. Neelam Pandit), brother Arunesh and my family members for their unconditional trust and support.

NEERAJ KUMAR PANDIT

Dedication

This thesis is dedicated to my parents.

Abstract

Cost-efficient electrocatalysts to replace precious platinum group metals (PGMs)-based catalysts for the hydrogen evolution reaction (HER) carries significant potential for sustainable energy solutions. Machine learning (ML) methods have provided new avenues for intelligent screening and predicting efficient heterogeneous catalysts in recent years. We coalesce density functional theory (DFT) and supervised ML methods to discover earth-abundant active heterogeneous NiCoCu-based HER catalysts. An intuitive generalized microstructure model was designed to study adsorbate's surface coverage and generate input features for the ML process. The study utilizes optimized eXtreme Gradient Boost Regression (XGBR) models to screen NiCoCu alloy-based catalysts for HER. We show that the most active HER catalysts can be screened from an extensive set of catalysts with this approach. Therefore, our approach can provide an efficient way to discover novel heterogeneous catalysts for various electrochemical reactions.

Table of Contents

List of Figures

CHAPTER 1

CHAPTER 2

CHAPTER 3

CHAPTER 4

List of Tables

CHAPTER 1

CHAPTER 2

CHAPTER 3

CHAPTER 4

APPENDIX - A

Acronyms

AI	Artificial Intelligence
ASE	Atomistic Simulation Environment
DFT	Density Functional Theory
fcc	face-centered cubic
GGA	Generalized Gradient Approximation
GPAW	Grid-based Projector Augmented Wave
GPR	Gaussian Processes Regression
hcp	hexagonal close-packed
HER	Hydrogen Evolution Reaction
HF	Hartree-Fock
KRR	Kernel Ridge Regression
LDA	Local Density Approximation
ML	Machine Learning
PAW	Projector Augmented Wave
PBE	Perdew-Burke-Ernzerhof
PGM	Platinum Group Metal
RBF	Radial Basis Function
RMSE	Root Mean Square Error
SVM	Support Vector Machine
SVR	Support Vector Regression
XGBR	eXtreme Gradient Boosting Regression
ZPE	Zero-point Energy

CHAPTER 1

1. Introduction

The world is facing an energy paucity, as the restricted pool of fossil fuels, natural gas, and other conventional energy sources have failed to serve demand unconditionally. The prices of these limited resources have hit multi-year highs recently. The cause of this surge in demand for energy across the globe has landed us in a state where we are seeking an eco-friendly option for energy resources. According to recent statistics, total installed renewable power capacity grew nearly 10% to reach 2,839 GW globally in 2020. *[1]* The ongoing efforts to overcome this demand beyond fossil fuels have sought one of the ways in the form of hydrogen. Hydrogen and energy have been seen together for a long time; being a clean fuel fulfils every requirement. It offers exceptionally high energy density and produces no direct pollutants or greenhouse gases emission. Nevertheless, to significantly contribute for clean energy transitions, hydrogen should be adopted in all possible sectors. Electrochemical water splitting offers the best of both worlds, generating hydrogen and oxygen in a clean way.

1.1. Hydrogen Evolution Reaction (HER)

The hydrogen evolution reaction (HER) incorporates two essential steps: the adsorption of individual hydrogen (H) atoms and then getting desorbed as a hydrogen molecule (H_2) from the electrode's surface. As illustrated in Figure 1.1, the adsorption step pertains to the Volmer reaction, which gives adsorbed hydrogen on electrode metal surface (M-H*) by proton reacting with an electron in the given medium. Consequently, anyone or both can proceed with the desorption step among Heyrovsky and Tafel reactions. The

Heyrovsky reaction is an electrochemical reaction where the adsorbed hydrogen reacts with another similar adsorbed hydrogen atom to generate the molecule. In the Tafel reaction, two adsorbed hydrogen atoms come up as a molecule from the electrode's surface without any electron. The HER can occur in both acidic and alkaline mediums. However, the proton source will be the hydronium cation (H_3O^+) in an acidic medium, whereas the water molecule itself provides it in an alkaline medium. Even though water electrolysis is the most demanding solution, it is thermodynamically unfavorable ($\Delta G° = 237.178$ kJ mol^{-1}) *[2]* and demands an efficient electrode material characterized by higher intrinsic activity to reduce the overpotentials.

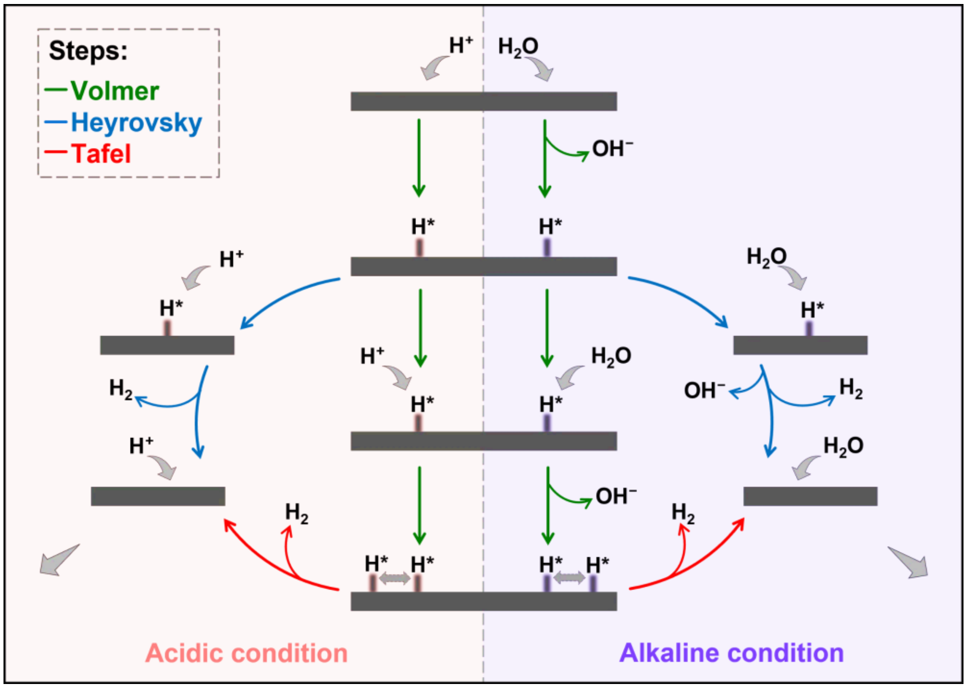

Figure 1.1: Schematic representation of the hydrogen evolution reaction (HER) in acidic and alkaline medium, proceeded by Volmer, Heyrovsky, and Tafel steps.

1.2. Heterogenous Catalysts

The Sabatier principle *[3]* states the catalytic efficacy by an optimum association for an efficient catalyst with the reactant. On the experimental side, the volcano plot illustrates the principle by representing catalyst activity against its reactivity. *[4]* The PGMs being at the summit of the Sabatier volcano plot with optimum hydrogen binding energy and exceptionally high exchange current density show benchmark performance for the HER, maintaining an optimum Gibbs free energy of H atom adsorption. *[5]* Nonetheless, their low abundance and excessive cost deter their universal application. However, efficient, low-cost, and earth abundant HER catalysts are crucial enablers for water electrolysis that produces H_2 with minimal resource consumption. *[6]*

Prior studies have discovered several catalysts for the HER using PGMs with earth abundant metals in different ratios. *[7-9]* But to cut down the cost of a catalyst effectively, we need to consider purely abundant alternatives. Along with the present catalysts, first-row transition metals with numerous format *[10-13]* have also attracted the scientific community to explore their possible contribution to HER. So, to explore and offer some alternative verticals in this aspect, we have chosen Ni, Co, and Cu metals for our alloys system. We have selected three earth-abundant metals (Co, Ni, and Cu), in agreement with the Sabatier principle, foreseeing comparable catalytic efficiency as Pt for HER. Although Ni and Ni-based alloys are less active than Pt, they have been proven to perform well for HER. Ni can be studied further to have a potential catalyst that can deliver similar performance to PGMs-based catalysts. The Ni-based electrode materials show minimum free energy of hydrogen adsorption (ΔG_{H^*}) and maximum exchange current density among all the present non-noble metals. As previously reported by Miles et al., Ni has the best performance among non-noble metals. *[14, 15]* Hence, it can be one of the promising candidates for HER. As a consequence, Ni has attracted a significant part of the research community to find an economical way for HER. *[16]* Considering this, we have taken Ni as our base metal. Moreover, Co is nearly alike in performance with Ni, at every pH as reported by Asefa and co-workers. *[17]* Furthermore, there are studies on Co, Co-Ni, *[18]* Co-Cu, *[19]* Co-oxides, *[20]* and other Co-based alloy materials for the HER. *[21, 22]* On the other hand, Cu lying on the weak adsorption slope in the volcano plot, Cu, Cu-Ni, *[23]* and other Cu-based electrocatalysts have also been tested in various forms for hydrogen evolution. *[24, 25]* Furthermore, the NiCoCu-based nanotubes arrays have already been investigated experimentally for non-enzymatic glucose sensor electrode material. *[26]* Also, there are previously reported characterization studies on NiCoCu-based thin films and multilayer nanowires, *[27, 28]* supporting the feasibility of our alloy system to some extent. Considering the crucial role of weak adsorption nature of the alloy particularly for the H_2 molecule desorption stage in the HER, we have chosen Ni, Co, and Cu based catalysts along with their all-possible alloy-based special combinations due to their compelling abundance and catalytic performance for HER. Therefore, we believed that their similar atomic radii, properties, and synergistic effect can lead to a significant activity towards HER. We have considered the periodic fcc(111) facet for our NiCoCu-based alloy systems while it has been reported that the periodic Ni fcc(111) surface has the satisfactory binding energy during the adsorption of hydrogen atoms as well as desorption of hydrogen molecules. Moreover, on the Ni(111), H from the O–H bond dissociation is closer to the adjacent Ni atom. *[29]*

1.3. Artificial Intelligence (AI)

Artificial intelligence (AI) belongs to the field of computer science. It is the intelligence exhibited by computer machines, similar to the natural intelligence possessed by animals, including humans but with the edge of high computational capability.

The AI was first introduced by the British mathematician Alan Mathison Turing through his groundbreaking work, “Computing Machinery and Intelligence,” published in 1950. *[30]* Later with enormous advancements in the field, its further subsets; machine learning (ML), and deep learning (DL) methods were established.

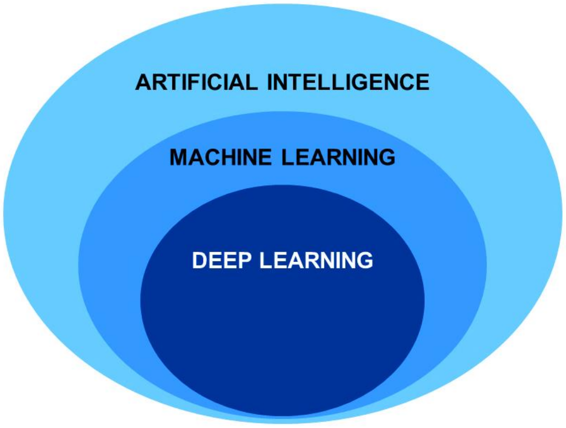

Figure 1.2: Domain representation of artificial intelligence, machine learning, and deep learning.

1.3.1. Machine Learning (ML)

Being the subset of AI, machine learning (ML) was first introduced in 1959 by Arthur Lee Samuel, an American computer scientist. He defined ML as the field of study that allows computers to learn without explicitly programming. That can be tooled for problems that demand a lot of fine-tuning and rapid adaptation.

The ML methods’ ascendancy has been breathtaking due to the dramatic advancements in data science and computer science technologies. That has fascinated many other fields and communities after realizing its potential uses. ML applications in chemistry have a significant impact and are believed to have much more advancement in the forthcoming years. Due to deficiency of data, smaller data sets are mainly used in this field and offer two typical approaches: “supervised” and “unsupervised” learning.

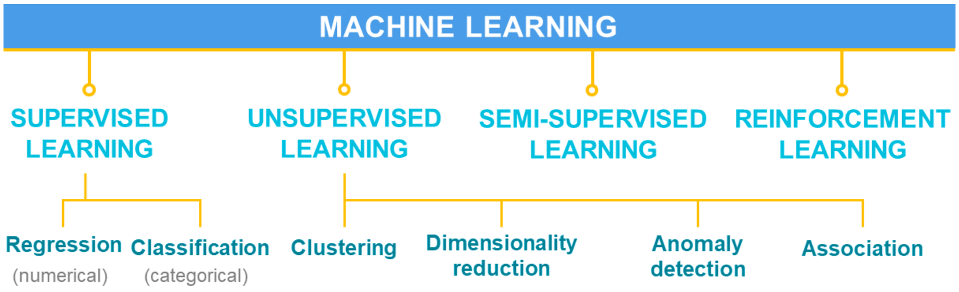

Figure 1.3: Different types of methods in machine learning.

1.3.1.1. Supervised Learning

Supervised learning methods exclusive to regression and classification algorithms require the training of an algorithm to map inputs to a specific output in the data set and provide fundamentally optimized performance based on experience. Lately, supervised regression models have been successfully tuned and applied to predict adsorption energies concerning heterogeneous catalysts. These methodologies provide efficient, prompt solutions for screening active and selective catalysts, being thrifty for the time and cost of their study. Moreover, the adsorption energy has been observed as a prominent descriptor for the catalyst's activity in previously reported studies, using supervised learning techniques. *[31-36]*

1.3.1.2. Features

Features are the essential measurable variables of the entity which is being studied. Features in ML are the most crucial segment of the datasets. They are intended to provide the necessary information for the undertaken numerous conditions. To enhance the quality of the features for the considered dataset, one can employ methods like feature selection and feature engineering. Features are generally numeric or strings. Nevertheless, they can have other formats as well.

1.3.1.3. ML models

Numerous ML models are presently available, categorized in the above-discussed ML methods. Particularly for the supervised regression techniques, some of the prominent ML models are Linear Regression, Kernel Ridge Regression (KRR), Support Vector Regression (SVR), Gaussian Process Regression (GPR), and eXtreme Gradient Boosting Regression (XGBR). All these ML models are free to access and are available at scikit-learn *[37]* and XGBoost *[38]* with their complete uses and installation details. However, a brief discussion for considered models have been done below:

- **Linear Regression:** The LinearRegression model simply performs data fitting based on a linear association between the target label (output value) and the input features. The predictions by linear regression model are derived by an equation (1.1)**,** where it computes a weighted sum of the input features ($\theta_0, \theta_1, \theta_2 \cdots \theta_n$) with an added bias constant (θ_0).

  $$\hat{p} \;=\; \theta_0 + \theta_1 f_1 + \theta_2 f_2 + \cdots + \theta_n f_n \tag{1.1}$$

  where, $\hat{p}$ denotes the predicted value, θ_i is the *i*th parameter of the model, f_j is the *j*th feature value, and *n* is the number of features.

- **Kernel Ridge Regression (KRR):** Kernel Ridge Regression is a combination of ridge regression and the kernel trick. It uses the squared error loss function for understanding the functions in the space induced by taken kernels and the data. The loss function for ridge regression can be written as:

  $$\Gamma(\theta) = MSE(\theta) + \alpha \frac{1}{2}\sum_{i=1}^{n} \theta_i^2 \tag{1.2}$$

  The first term is the mean squared error gradient vector and second term is the regularization term, which does the data fitting while maintaining the least possible model weights.

- **Support Vector Regression (SVR):** The support Vector Machine algorithm is a protean model and supports both classification and regression type problems. The Support Vector Regression model tries to fit the maximum possible instances on the band plane while limiting desecrations. The epsilon (ϵ) hyperparameter restrains the band broadness. For the non-linear regression problems, kernelized SVM models can be used. Kernelized SVMs are helpful for employing a second-degree polynomial vector transformation (†) to a two-dimensional training set (α, β). Some commonly used kernels are linear, polynomial, radial basis function (RBF), sigmoid:

$$\text{Linear:} \quad \mathrm{K}(\alpha, \beta) = \alpha^{\dagger}\beta \tag{1.3.1}$$

$$\text{Polynomial:} \quad \mathrm{K}(\alpha, \beta) = (\gamma\alpha^{\dagger}\beta + r)^{d} \tag{1.3.2}$$

$$\text{Gaussian RBF:} \quad \mathrm{K}(\alpha, \beta) = \mathrm{e}^{(-\gamma\|\alpha-\beta\|^{2})} \tag{1.3.3}$$

$$\text{Sigmoid:} \quad \mathrm{K}(\alpha, \beta) = \tanh(\gamma\alpha^{\dagger}\beta + r) \tag{1.3.4}$$

- **Gaussian Process Regression (GPR):** GaussianProcessRegressor (GPR) is a robust kernel-based algorithm that employs a probabilistic model to perform regression. It uses Gaussian Process (GP) to project confidence for the predicted function. GPR adapts Bayesian approach implementing an adaptive probability distribution over all possible values, also termed as posterior distribution ($P(m|N)$).

$$P(m|N) = posterior = \frac{P(N|m) \times P(m)}{P(N)} \tag{1.4.1}$$

$$P(N) = \int P(N|m)P(m)dm \tag{1.4.2}$$

Among the kernelized GPR, RBF kernel (1.3.3) is very commonly used. Given that GPR models are good at understanding non-linearity in the data, RBF provides GPR with the similarity function by measuring the extent of instance matches with a certain landmark.

- **eXtreme Gradient Boosting Regression (XGBR):** eXtreme Gradient boosting (XGBR) is an optimized Gradient Boosting algorithm that performs sequent addition of predictors to an ensemble, supporting revamping its precursors. By employing second-order gradients and advanced regularization, it applies more accurate predictions. XGBoost follows log loss metric for classification problems, whereas it uses mean squared error (MSE) or mean average error (MAE) for regression models to assess the performance. It uses similarity score (S) for the gain of the root node calculation. The expression for similarity score can be written as:

$$S = \left(\frac{(\sum r_i)^2}{n+\lambda}\right) \qquad (1.5.1)$$

Where, $(\sum r_i)$ and n are the sum and the number of residuals, respectively. And λ is the L2 regularization term on weights. It can be implemented by mainly two algorithms; gbtree is a gradient descent of tree type, and gblinear is a regression boosting.

1.3.1.4. Testing and Validation

No doubt, these ML models are robust and advantageous. Nevertheless, we need to inspect how well the employed model has performed and predict the results unbiasedly. There is always a possibility that one model performs well for the provided known data but gives poor results on new input cases and is a case of overfitting and its reverse case is known as underfitting.

So, to avoid the poor performance of ML models, testing and validation is required. Testing and validation can be done by splitting a specific dataset into training and test sets. Here, the taken ML model can be trained with the training set and further tested by evaluating the predictions on the testing dataset. The model performing best in the test dataset can be considered for the final predictions.

1.3.1.5. Hyperparameter tunning

Each ML model has some parameters that define its architecture. These parameters are called hyperparameters and have been set with specific values as default. However, depending upon the nature of the data and the model's performance, they can be tuned to achieve the ideal performance. Hence, hyperparameter tuning is finding such values of the hyperparameters to have an optimized model according to one's data. Also, it must be noted that hyperparameters and model parameters are not the same as hyperparameters belonging externally, whereas model parameters are the internal part of the model and are independent of datasets.

Some of the often-used techniques for hyperparameter tuning are Manual Search, Grid Search, Randomized Search, Halving Grid Search, Halving Randomized Search, HyperOpt-Sklearn, and Bayes Search. These techniques are openly accessible at scikit-learn platform.

CHAPTER 2

---

2. Computational Methods and Approximations

2.1. Schrödinger Equation

The Schrödinger equation is the fundamental equation of quantum mechanics. Generally, the time-independent Schrödinger Equation is used to estimate the electronic structural properties of the materials and molecules. This time-independent form of Schrödinger equation can be expressed as equation (2.1).

$$H\Psi(r,R) = E\Psi(r,R) \tag{2.1}$$

Here, H represents the Hamiltonian operator, which defines all the properties of the system, Ψ represents the wave function of the system comprising all the information about the nuclei and electrons, and E represents the system's total energy. Solving the Hamiltonian of a system provides all the properties of that system. The Hamiltonian operator can also be expressed by equation (2.2) as follows,

$$H = -\frac{h^2}{2m_e}\sum_i \nabla_i^2 - \sum_I \frac{h^2}{2M_I}\nabla_I^2 + \frac{1}{2}\sum_{i\neq j}\frac{e^2}{|r_i - r_j|} + \frac{1}{2}\sum_{I\neq J}\frac{Z_I Z_J e^2}{|R_I - R_J|} - \sum_{i,j}\frac{Z_I e^2}{|r_i - R_I|} \tag{2.2}$$

Here in this equation, m_e and M_I are the mass of electron and nuclei, respectively. Whereas the r_i is the electron position and the R_I is the nuclei position. The Z_I is the nuclear charge of the considered system. The first and second terms in the equation represent electron and nuclei kinetic energy contribution, respectively. And the further three terms correspond to the electron-electron repulsion, nuclei-nuclei repulsion, and electron-nuclei attractive interaction.

Solving this differential equation for a many-body system can obtain its physically and chemically relevant ground state properties. Nevertheless, numerically solving this equation for real multi-electron systems is highly challenging and complex. Thus, we require approximations that can reduce the complexity without losing the accuracy.

2.2. Born-Oppenheimer Approximation

According to the Born-Oppenheimer approximation, the kinetic energy term for nuclei can be neglected because the mass of nuclei is much greater than that of an electron and is considered stationary compared to the electron. *[39]* With this first approximation, the Hamiltonian operator resulted into an electronic Schrödinger equation (2.3):

$$H = -\frac{h^2}{2m_e}\sum_i \nabla_i^2 + \frac{1}{2}\sum_{i\neq j}\frac{e^2}{|r_i - r_j|} + \frac{1}{2}\sum_{I\neq J}\frac{Z_I Z_J e^2}{|R_I - R_J|} - \sum_{i,j}\frac{Z_I e^2}{|r_i - R_I|} \qquad (2.3)$$

Even though the kinetic energy of nuclei term has been neglected, it is still not enough to reduce the time and complexity significantly. Therefore, the later approximations like Hartree-Fock (HF) theory and density functional theory (DFT) are more practical.

2.3. Hartree-Fock (HF) Approximation

The HF theory calculates the single reference Slater determinant using self-consistent methods. According to HF theory, the motion of a single electron is independent of the motions of the rest electrons and can be described as a one-electron wave function. The beginning of the Hartree Fock method is the Hartree approximation that states that the multi-electron wavefunction can be replaced by the product of the corresponding single-electron wavefunctions.

$$|\Psi(r_1, r_2, \dots r_N)\rangle \approx \Psi_1(r_1)\Psi_2(r_2) \dots \Psi_N(r_N) \tag{2.3}$$

But the straightforward Hartree wavefunction fails to satisfy antisymmetric condition for Fermions. For a two-electron system, the antisymmetry principle can be satisfied by the wave function like following type (2.4).

$$\Psi(x_1, x_1) = \frac{1}{\sqrt{2}}[\chi_1(x_1)\chi_2(x_2) - \chi_1(x_2)\chi_2(x_1)] \tag{2.4}$$

In case of multi electron systems, it can be written in a form of a single determinant, known as Slater determinant (2.5).

$$\Psi_{el} = \frac{1}{\sqrt{n!}}\begin{vmatrix} \psi_1(1) & \psi_2(1) & \cdots & \psi_n(1) \\ \psi_1(1) & \psi_2(1) & \cdots & \psi_n(1) \\ \cdots & \cdots & \ddots & \cdots \\ \psi_1(n) & \psi_2(n) & \cdots & \psi_n(n) \end{vmatrix} \tag{2.5}$$

Now the Hamiltonian can be simplified as,

$$\hat{H} = H^C + \frac{1}{2}\sum_{i \neq j} \frac{e^2}{|r_i - r_j|} \tag{2.6}$$

Where, the following core part of the Hamiltonian operator ($\hat{H}^C$) is exactly solvable.

$$\hat{H}^C = -\frac{h^2}{2m_e}\sum_i \nabla_i^2 - \sum_{i,I} \frac{Z_I e^2}{|r_i - R_I|} \tag{2.7}$$

The second part that accounts the repulsion of electrons which cannot be solved exactly. HF theory considers the electron-electron repulsion in an average way, by considering the independent motion of electrons. Therefore, by considering the Slater determinant one can obtain the state having lowest energy and optimization of the orbital using variation theorem leads to the lowest possible energy. The form of the HF equation is as follows (2.8):

$$f_i \chi_i = \epsilon_i \chi_i \tag{2.8}$$

In the above equation, χ_i is the eigen function and ϵ_i is the eigen value of the operator f_i, respectively. The energy eigen values are called as orbital energy of the system. The operator f_i is known as Fock operator which behaves like a one electron operator.

$$f_i = \widehat{H}^C + V_{HF}(i) \tag{2.9}$$

where, V_{HF} is the second term in the Hamiltonian that describes the electron-electron repulsion in average.

$$V_{HF}(i) = \sum_{i,I} \frac{Z_I e^2}{|r_i - R_I|} \tag{2.10}$$

The HF potential can be expanded in terms of coulomb operator J_i and exchange operator K_i according to the following equation (2.11).

$$V_{HF}(i) = \sum_{i} [J_i(x_i) - K_i(x_i)] \tag{2.11}$$

Where J_i signifies the classical repulsion among electrons and K_i denotes the exchange interaction which is generated from the anti-symmetric wave function nature. If one knows the eigen function χ_i then HF potential can be calculated using an iterative self-consistent field method starting with an arbitrary value of $V_{HF}(i)$. HF theory calculates the energy and other properties from the wave function of a system. For larger systems the wave function becomes too much complicated as it accounts three spatial as well as a spin coordinate for all the electrons. Hence, due to larger number of variables it is very difficult to apply HF theory on complex molecules. The total energy computed by the HF approach generally offers over 99% of the experimental value, but lots of essential interactions interesting for chemistry happen in the remaining 1%.

2.4. Density Functional Theory (DFT)

Density functional theory (DFT) a quantum-mechanical approach, which is used to find out the electronic structure and properties of the particular many body system by consideration of its electron density. This method is dependent only on three positional coordinates and hence, avoids the complexity of the wavefunction. This innovative idea is presented by Thomas-fermi, where ideal free electron gaseous molecules are used in the non-interacting system. Density functional models do not restrict to the exact solution of the Schrödinger equation and significantly lower the computation costs compared to either configuration interaction or Møller-Plesset models.

The DFT energy can be written as the sum of kinetic energy (E_T), the electron-nuclear potential energy (E_V), Coulomb (E_J), and exchange/ correlation energy (E_{XC}).

$$E^{DFT} = E_T + E_V + E_J + E_{XC} \tag{2.12}$$

Here, all terms except E_T depend on the total electron density, $\rho(\boldsymbol{r})$:

$$\rho(r) = 2 \sum_{i}^{orbitals} |\psi_i(r)|^2 \tag{2.13}$$

The ψ represents the orbitals, analogous to molecular orbitals in HF theory. P. C. Hohenberg and W. Kohn have also proposed two theorems which are highly useful for the DFT calculations. The discussion on them have been given in the below section. *[40, 41]*

2.4.1. The Hohenberg-Kohn Theorems

Theorem 1: According to this theorem for multi electron system, the ground state energy is the electron density *ρ(r)* functional of the interacting electrons moving under the external potential of V_{ext}, implying:

$$E = E_v[\rho] = T[\rho] + V_{ee}[\rho] + V_{ext}[\rho] \tag{2.14}$$

$T[\rho]$ and $V_{ee}[\rho]$ denotes the kinetic energy and the electron-electron interaction potential functional, respectively. Whereas V_{ext} is the external potential given as,

$$V_{ext} = \int u(r)\rho(r)dr = \sum_{A=1}^{N} \frac{Z_A}{r_{iA}} \tag{2.15}$$

Theorem 2: The second theorem states that the system's ground state energy can be achieved variationally and the electron density which minimizes the total energy is the correct ground-state density. Moreover, minimum energy can be achieved by considering the exact density of ground state. The kinetic energy and interaction potential functionals can be established by decreasing the energy with respect to variation in $\rho(r)$.

$$E_v[\rho] \geq E_v[\rho_0] \tag{2.16}$$

However, there were no proper ways for the ground state density calculation of a system in the above-mentioned theorems. Later W. Kohn and L. J. Sham formulated the Kohn-Sham equation after which the actual application of Hohenberg-Kohn theorems begins to carry out DFT calculations.

2.4.2. Kohn-Sham Formulation

W. Kohn and L. J. Sham formulated new set of equations for the Hohenberg-Kohn theorems application. As per this formulation, the complexities in many-body problem can be reduced to non-interacting particle problem. Where, the single particles can be defined by an effective potential $V(\boldsymbol{r}_i)$, termed as Kohn-Sham potential. The total ground state energy can be described as:

$$E[\rho(r)] = T_0[\rho(r)] + \frac{1}{2}\iint \frac{\rho(r)\rho(r)'drdr'}{|r-r'|} + \int V_{ext}(r)\rho(r)dr + E_{xc}[\rho(r)dr] + E_{II} \tag{2.17}$$

Where, the first term denotes non-interacting electrons' kinetic energy; the second term describes the classical electron-electron Coulomb interaction (Hartree energy); the third term is the interaction potential between valence and core electrons; the fourth term considers all the non-classical many-body effects between electrons (exchange-correlation interaction); and the last term describes the nuclei-nuclei interaction. Now, the above equation can also be written as:

$$\left[-\frac{1}{2}\nabla^2 + V_{eff}(r)\right]\Psi_i(r) = \mathrm{E}_i\Psi_i(r) \tag{2.18}$$

Where $\Psi_i(r)$ denotes the Kohn-Sham orbitals in place of wave function, whereas V_{eff} can be written as:

$$V_{eff} = V_{Hartree} + V_{ext} + V_{xc} \tag{2.19}$$

Consequently, the effective potential can be described by the external potential, Coulomb interaction, and the exchange correlation interaction. And if one knows the exchange correlation potential then it is possible to solve many-body problem. Still, the exchange correlation interaction is challenging to solve, therefore different approximations are used to solve this problem. The following approximations are broadly used for the simulation of molecular as well as solid state problems. *[42]*

2.4.3. Exchange-correlation Functional

As the exchange correlation potential is not easy to solve, some approximate methods to ease the DFT calculations are required. The exchange-correlation functional $E_{xc}(\rho(r))$ can be divided into two parts as exchange and correlation, can be defined as:

$$E_{xc}(\rho(r)) = E_x(\rho(r)) + E_c(\rho(r)) \tag{2.20}$$

The exchange correlation energy functional $E_{xc}(\rho(r))$ can be approximated by some local functional based on the electron density.

2.4.4. Local Density Approximation (LDA)

In LDA, Hohenberg and Kohn approximated the exchange correlation energy locally from homogeneous electron gas of identical density. *[43, 44]* Hence, LDA depends only on the local density i.e., the exchange correlation energy can be expressed like,

$$E_{xc}^{LDA} = \int \rho(r)\varepsilon_{xc}(\rho)dr \tag{2.21}$$

$$u_{xc} = \varepsilon_{xc}[\rho(r)] + \rho(r)\frac{\partial \varepsilon_{xc}[\rho]}{\partial \rho} \tag{2.22}$$

where $\varepsilon\varepsilon_{xc}(\rho)$ represents the exchange-correlation energy density related to the homogeneous electron gas of density $\rho(r)$. Although, LDA produces quite good results for solids, it is not great for molecules.

2.4.5. Generalized Gradient Approximation (GGA)

GGA is the most commonly used exchange correlation functional in present time. Along with electron density it accounts the gradient of electron density that leads the exchange correlation energy to,

$$E_x^{GGA}\left[\rho^\alpha, \rho^\beta\right] = \int f\left[\rho^\alpha(r), \rho^\beta(r), \nabla_{\rho^\alpha(r)}, \nabla_{\rho^\beta(r)}\right] dr \qquad (2.23)$$

These functional significantly reduces the over binding error in LDA. Some commonly used important GGA functionals are Perdew, Burke and Ernzerhof (PBE), Perdew and Wang (PW91), PBEsol and revised PBE (RPBE). *[45-48]*

2.5. Basis Sets

Basis sets are a set of one particle functions those applied to define the molecular orbitals of any system. There is a set of basis functions for each and every atom in a molecule to guess its orbital. On the basis of the functional used to define, they can be categorized as: Slater type orbitals (STO), Gaussian type orbitals (GTO), Effective core potential (ECP), Plane wave, and other. Herein, we have used plane wave basis sets due to considering the periodic systems in our study.

2.5.1. Projector Augmented Wave (PAW) Method

The electrons residing in core and valence orbital have different interactions due to distinct distances of core and valence electrons with nuclei. As a result, the core electron wave functions oscillate rapidly whereas the valence electron wave functions are smooth. For the electrons outside the augmented region, we can consider the plane wave basis sets. Nevertheless, describing the core electron wave functions is challenging with plane waves due to high computational cost. Hence, a partial wave expansion is used to describe the core electrons and it converts the rapidly oscillating wave functions to smoother one. This technique is based on the linear transformation operator (T) and termed as PAW method. *[49-52]* The all-electron wave function $\widetilde{\Psi}_n$ to be replaced by a pseudo wave function $\widetilde{\Psi}_n$ such that

$$|\Psi_n\rangle = T\left|\widetilde{\Psi}_n\right\rangle \tag{2.24}$$

Where, T is the transformation operator and both $|\Psi_n\rangle$ and $\left|\widetilde{\Psi}_n\right\rangle$ are expressed with a linear combination of partial waves for each augmentation regions.

$$|\Psi_n\rangle = \sum_i c_i\,|\phi_i\rangle \tag{2.25}$$

$$\left|\widetilde{\Psi}_n\right\rangle = \sum_i c_i\,\left|\widetilde{\phi}_i\right\rangle \tag{2.26}$$

The transformation operator, T is defined as

$$T = 1 + \sum_i \left(|\phi_n\rangle - \left|\widetilde{\phi}_n\right\rangle\right)\langle\tilde{p}_i| \tag{2.27}$$

Here $\langle\tilde{p}_i|$ is called projection function. Hence, pseudopotential helps to get rid from the problem of core and valence electrons. However, PAW is combined with ultra-soft pseudopotentials and augmented-plane-wave.

2.6. GPAW and ASE

Grid-Based Projector Augmented Wave (GPAW) *[53, 54]* is an open-source application for first-principles calculation based on the PAW method with a supported interface of the atomic simulation environment (ASE). *[55]* GPAW calculations are managed through command scripts, majorly written in the programming language Python.

2.7. Computational Details

The Grid-Based Projector Augmented Wave (GPAW) code was used to perform all the DFT calculations using the Projector Augmented Wave (PAW) method as the wave functions. The Perdew–Burke–Ernzerhof generalized gradient approximation (GGA-PBE) *[46, 47]* functional was chosen for the exchange-correlation potential, implemented in the Atomistic Simulation Environment (ASE). As illustrated in Figure 2.1, a periodic 4 × 4 × 4 atoms Ni(111) surface slab was considered for the adsorption energy calculations and further studies.

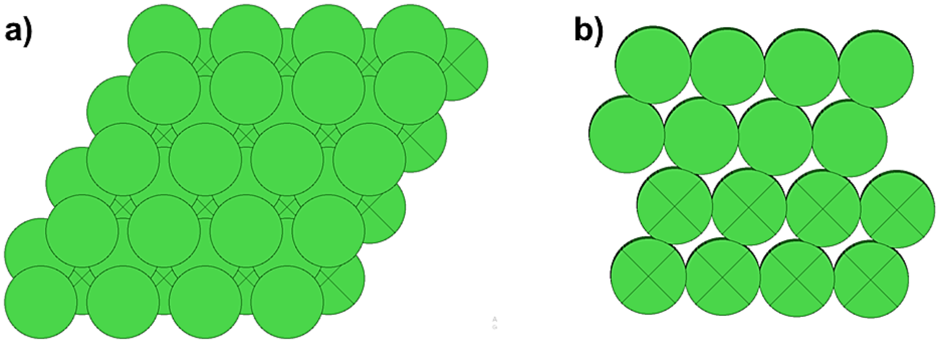

Figure 2.1: The 4 × 4 × 4 periodic Ni(111) slab model: a) top and b) side view. The crossed spheres of the lower two layers signifies the fixed state, and uncrossed spheres represents the relaxed state for the further calculations.

A plane-wave cutoff of 400 eV has been considered for plane-wave expansion of the electronic wave function. Our group has previously verified similar cutoff values for CO_2 reduction reaction using high entropy alloy-based systems. *[33]* Hence, considering the presence of oxygen during the complete HER, which has an almost similar potential of 400 eV, it is sufficient for the calculations. The average lattice parameter of the constituent metals was chosen according to Vegard's law. *[56]* We have considered the lattice parameter of Ni (Table A1 in appendix - A) for the system, being the base metal in the slab system for the calculation purpose. The Davidson (DAV) method eigensolver has been used throughout the calculations for iterative diagonalization of the Kohn-Sham Hamiltonian, with the Monhorst-Pack k-point sampling of the Brillouin zone of (4,4,1). A ~20 Å vacuum region was added to the periodic slab along the z-direction to exclude all the periodic image interactions. The lower two layers were fixed, and the upper two layers were allowed to relax during geometry optimizations with the force minimization convergence criterion of 0.09

eV/Å. Additionally, all the calculations were performed, taking the respective magnetic moments of the metals under account for the system consisting of them. The following equations (2.29 and 2.30) have been used to calculate the adsorption energies of H (ΔE_H) and H_2 (ΔE_{H_2}):

$$\Delta E_H = E_{H^*} - \left(E_s + \frac{1}{2} E_{H_2} \right) \tag{2.28}$$

$$\Delta E_{H_2} = E_{H_2^*} - \left(E_s + E_{H_2} \right) \tag{2.29}$$

where E_{H^*} and $E_{H_2^*}$ are the respective DFT energies of the relaxed slabs in the presence of the adsorbate H and H_2, respectively. Moreover, E_s is the DFT energy of the slab in the absence of adsorbate, and E_{H_2} is the DFT energy of the molecular gas-phase references. The computational hydrogen electrode model *[57]* has been considered for the molecular gas-phase references as described by Nørskov and co-workers.

CHAPTER 3

---

3. Results and Discussion

Primarily, we have constructed a 64 atoms Ni(111) slab with 16 atoms in each 4 layers of the slab (4 × 4 × 4). Within the upper two layers of the 64 atoms slab, we presented a microstructure model by considering the neighboring atoms of the adsorption sites and selecting the input features to perform supervised ML. For this, training data of 63 structures were prepared through computed DFT values with the corresponding 12 surface microstructural features. After that, feature importance toward the output has been determined to understand the relation between features and the output data (adsorption energy). Then, several supervised regression models have been optimized with hyperparameter tuning on training data and evaluated with the test data to achieve the best model for the prediction. Finally, with the adsorption energies of all 5400 structures, active catalysts have been screened in using adsorption energies of the exact slab model of pure Pt metal with its comparable systems.

3.1. Microstructure Modeling

The adsorption of H atom(s) can majorly occur on four possible sites: hollow-hcp, hollow-fcc, bridge, and on top. Earlier studies have found that the site preference of H^* adsorption on the Pt(111) surface has a trend of hollow-fcc > on-top > hollow-hcp > bridge. *[58, 59]* In agreement with these sites' preferences, four cases of adsorption were considered (Figure 3.1). First two cases were single H atom adsorption at individual hcp and fcc hollow sites, respectively. In the third case, we have considered the adsorption of two single H atoms at adjacent hollow hcp and fcc sites to study the adsorbate's least possible coverage effect over proposed catalytic surfaces. Furthermore, the H_2 molecule adsorption has been considered at the metal on-top site *[60]* as the fourth case. These four cases can address the possible significant stages involved in the HER which can describe the real scenario of this process including surface coverage effect. With these adsorption possibilities and all metal combinations in the alloy slab system, it would have been challenging to perform calculations and examine the proposed system without following any explicit direction. Therefore, the concept of microstructure modeling has been adopted in this work with reference to the previous works reported by our group *[33]* and others. *[31, 32]*

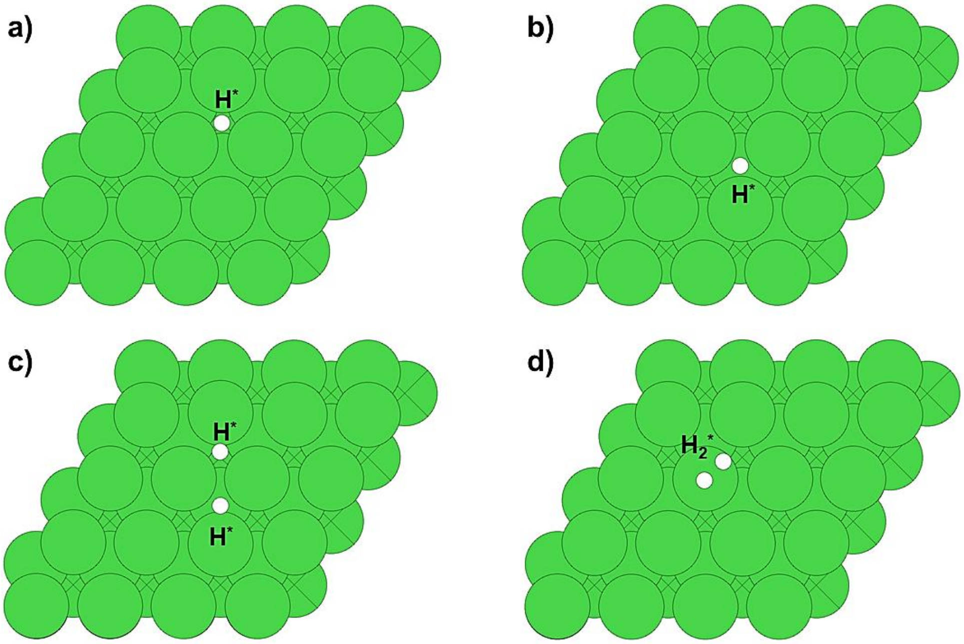

Figure 3.1: Possible adsorption cases for adsorbate(s) at considered sites: a) H^* at hollow fcc, b) H^* at hollow hcp, c) $2H^*$ at hollow hcp-fcc, and d) H_2^* at metal ontop.

The adsorption energy can be distinguished by the elemental labels and atomic positions relative to the adsorbate for a given system surface. Given the chemical environment in the adsorbate's vicinity is majorly concerned with the type of atoms present at the first and subsequent layers of the catalytic surfaces, descriptive features to demonstrate the catalytic surface environment is incredibly important. In this context, the microstructure model of the present study is unique, it was deemed helpful for the adsorbate's coverage effect study. As depicted in Figure 3.2, we have considered a standard microstructure model from 11 atoms within the upper two-layer of the slab system to assess the influence of metal position on the surface coverage and their preference for the adsorption energies. The microstructure model has been further preferentially classified into four regions based on the extent of impact they have resulted during the adsorption of the adsorbate in a particular chemical environment. The two metal atoms in the first region have maximum scope of interaction during hollow hcp and fcc site H^* adsorption. Then the following two atoms in the second region have a relatively lower scope of interaction than first region. The third region consisting of four atoms from the first layer, has less interaction than second region. And the fourth region incorporates three atoms from the slab's second layer, possessing the least scope of interaction among other regions with the adsorbate during the HER.

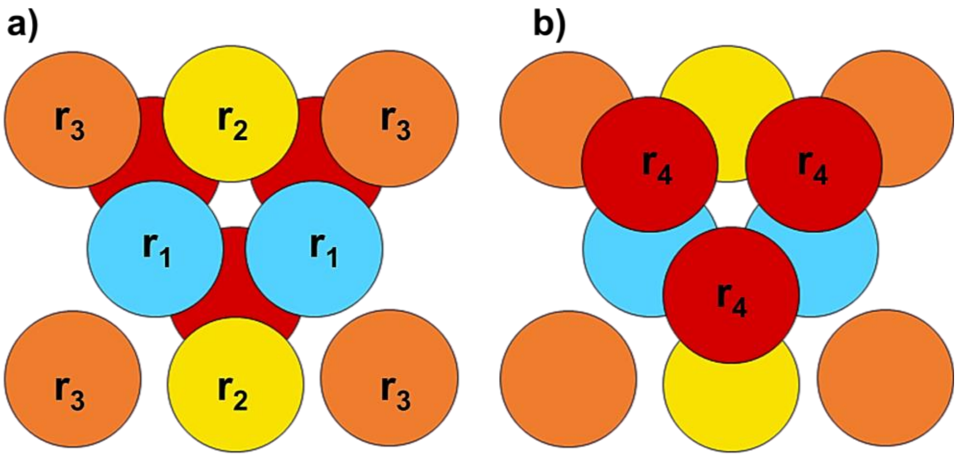

Figure 3.2: Comprehensive microstructure model for the considered adsorption sites a) top view, and b) bottom view. The 1st, 2nd, 3rd, and 4th

regions are represented by blue, yellow, orange, and red spheres, respectively. Here r_1, r_2, r_3, and r_4 represents region 1, 2, 3, and 4, respectively.

The 5400 possible combinations, resulted from pure, bimetallic, and trimetallic (among Ni, Co, and Cu) combinations within four regions of the microstructure model consisting of 11 atomic positions. The rest 53 among 64 atoms are Ni metals. The utilized combination expression and detailed calculation can be found in the appendix - A (Text A1). Performing DFT calculation for such large combinations is practically impossible even with the fastest ab initio tools and is the primary cause for using ML in this work.

3.1.1. Input Features Selection

Consequently, we have used the microstructure indexes as 12 input features in the supervised ML models, labeled with adsorption energy as the output values. The considered set of 12 input features consists of 3 features from each four regions of the designed microstructure model (Figure 3.3). While these features can describe the surface environment type, but certainly cannot provide the exact location of each metal atom within the regions. An illustrative example is given in the Figure 3.4. These sets of features are informative enough to provide insight into that chemical environment. However, the specific metal-wise locations cannot be determined with the considered set of features as the feature properties are associated with the region and not with the exact atomic locations.

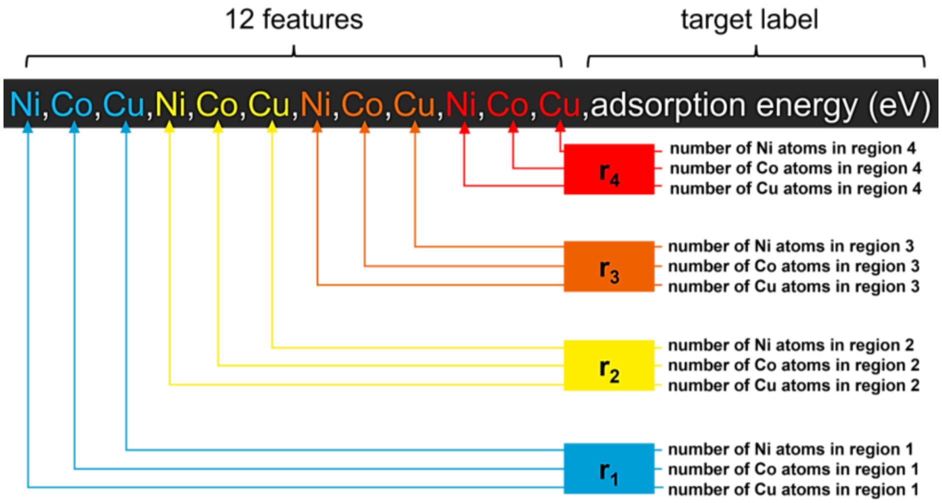

Figure 3.3: Description of input features on microstructure model for ML; The 12 features set represents the type and number of metal atom(s) present in each of the region. The first 3 features signify the type and number of metal atom present in the region 1, followed by region 2, 3 and 4.

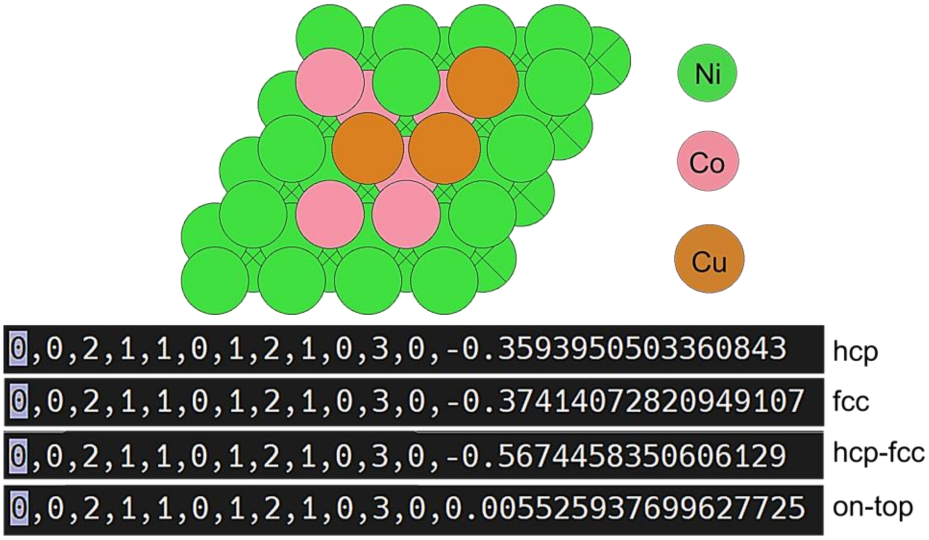

```
0,0,2,1,1,0,1,2,1,0,3,0,-0.3593950503360843
0,0,2,1,1,0,1,2,1,0,3,0,-0.37414072820949107
0,0,2,1,1,0,1,2,1,0,3,0,-0.5674458350606129
0,0,2,1,1,0,1,2,1,0,3,0,0.005525937699627725
```

Figure 3.4: Illustrative example of a taken set (trimetallic) of features of microstructure model. These combinations were used to prepare training dataset for performing machine learning.

3.2. Training Data Set Preparation

Input features are the cornerstone for training the ML model with labeled adsorption energies. Herein, supervised regression ML models were used to achieve the adsorption energy values of all 5400 combinations. We have reduced a significant amount of time with the help of DFT-calculated adsorption energies of well-sampled 63 structures (consisting of 3 pure, 30 bimetallic (bm), and 30 trimetallic (tm) microstructures) and their corresponding surface microstructures as input for our ML regression models. Drastic differences have been considered in combinations while choosing 63 (more than 1%) out of 5400, intended to provide a complete insight of all combinations as a whole. In addition to that, a region wise variety of metal types have been taken in order to have the most diverse selections. Training data is an essential component in any ML task, as the predictions rely on how well-acquainted one's ML model is with the targeted dataset. Four separate sets have been generated for adsorption energy values at hollow-hcp, hollow-fcc, hollow-hcp-fcc, and on-top sites, corresponding to the same set of 12 features, representing chosen 63 microstructures. Initially, the ML models were evaluated with the help of bifurcating the computed DFT data set in an 80:20 ratio for the training and testing, respectively. The root-mean-squared error (RMSE) values with the predicted and test data have been used to inspect the prediction performance of respective ML models. The RMSE values for all considered optimized ML models for all four data sets have been calculated using equation 3.1 (where $\mathrm{X_i}$ represents the actual DFT calculated adsorption energies, $\mathrm{x_i}$ represents the predicted adsorption energies, and N is the number of non-missing data points).

$$\mathrm{RMSE} = \sqrt{\frac{1}{\mathrm{N}}\sum_{\mathrm{i}}^{\mathrm{N}}(\mathrm{X_i} - \mathrm{x_i})^2} \tag{3.1}$$

The values were satisfactory enough for the complete data set prediction and have been tabulated in the appendix - A (Table A2).

3.3. ML Model Selection

Five supervised ML regressors have been considered for the prediction. We have tried employing ordinary Linear regression and some kernel-based algorithms like Kernel Ridge Regression (KRR), Support Vector Regression (SVR), Gaussian Process Regression (GPR), implemented in the scikit-learn package. *[37]* Gradient Boosting framework such as eXtreme Gradient Boosting Regression (XGBR) *[38]* has also been used. All the algorithms used are available at their respective open-source libraries. In this study, we have considered two ML methods. ML1 type methods are performed with the individual datasets of considered four adsorption sites and have been represented by ML1hcp, ML1fcc, ML1hcp-fcc, and ML1on-top. Whereas in ML2 type method, all four datasets of the adsorption sites have been merged into a single data set with an additional 13th feature in the input feature set.

3.3.1. Model Optimization

However, these algorithms are available with their default parameters which can be tuned according to the user. We have adjusted the hyperparameters of these algorithms by employing two prevalent techniques, RamdomizedSearchCV and GridSearchCV, both implemented in the scikit-learn package. With this, we were able to achieve the best possible values of hyperparameters, resulting in optimized algorithms. Each model's training and testing have been performed with the train and test data set, followed by RMSE evaluation. As it happens in ML, for a specific set of data, one optimized algorithm performs relatively better with the least RMSE than the rest and can be used for the best possible predictions. After obtaining RMSEs for all considered optimized regressors, we have used the best individual models for each data set for the complete prediction.

3.3.2. Prediction Evaluation

We have found that the optimized XGBR has the least test RMSE values (Figure 3.5) 0.0151 eV, 0.0108 eV, 0.0244 eV for hcp, fcc, and on-top data set, respectively, among other optimized algorithms. At the same time, the optimized SVM has performed better with a Test RMSE of 0.2584 eV (Figure 3.5c) in the case of the hcp-fcc data set. RMSE values of all optimized algorithms for all four data sets can be found in the appendix - A (Table A2) with their respective optimized values of hyperparameters.

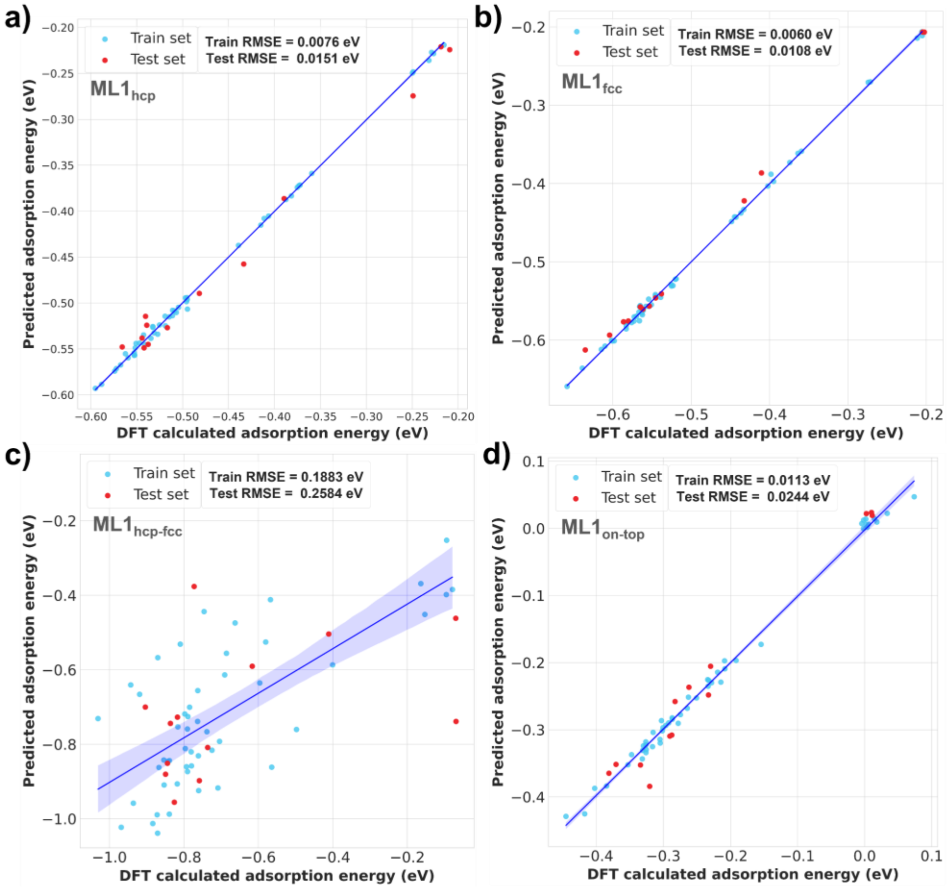

Figure 3.5: Plots of DFT calculated adsorption energies (ΔE_{calc}) versus predicted adsorption energies (ΔE_{pred}) with their respective indicated test and train RMSE values: a) hollow hcp site with optimized XGBR model, b) hollow fcc site with optimized XGBR model, c) both, hollow hcp-fcc site with optimized SVR model, and d) on-top site with optimized XGBR model. ML1 represents the method 1 by considering individual datasets.

Our DFT calculated adsorption energies were less diverse; however, as discussed in the previous section, we have tried with the well-sampled 63 training dataset to represent the complete 5400 microstructural combinations overall. While we found the performance of our models satisfactory and acceptable, the obtained RMSE for the optimized SVR model in the case of hcp-fcc (Figure 3.5c) is slightly high, compared to performance of rest three site adsorption cases, underlying the complexity and diverse nature of obtained calculated adsorption energies.

This is due to the increased possible number of Cu metal atoms, dominating the first three regions of the microstructure model while considering all the combinations. While some systems (slab with adsorbates) were being optimized, the adsorbates got migrated from their initial expected sites in the case of Cu populated microstructural regions. Analyzing the optimized structures of our sample set, we have observed the adsorption of H^* atoms at hcp-fcc adjacent hollow sites got changed from the expected one due to the less adsorbing nature of the present Cu metal atom. Similar cases were also observed in H_2^* adsorption at the on-top site. Here, the adsorbates were found already desorbed in the final optimized system with adsorbate and slab, only in cases where Cu was present for the on-top site metal. Nevertheless, since only one metal atom (on-top) had a significant role in affecting the adsorption here, the results did not vary much unlike in case of two H^* coverage at hcp-fcc. However, in an attempt to improve the performance of our ML model, we merged all four data sets (hcp, fcc, hcp-fcc, and on-top) into one set of 252 data with an added 13th feature for describing the type of site against the DFT calculated adsorption energies (Figure 3.6). Since the type of site is a categorical variable, we have adapted the label encoding method to handle this categorical attribute. Based on the average values of the 63 DFT-derived adsorption energies for site-wise datasets per adsorbate atom, we encoded the fcc, hcp, hcp-fcc, and on-top with 0, 1, 2, and 3, respectively.

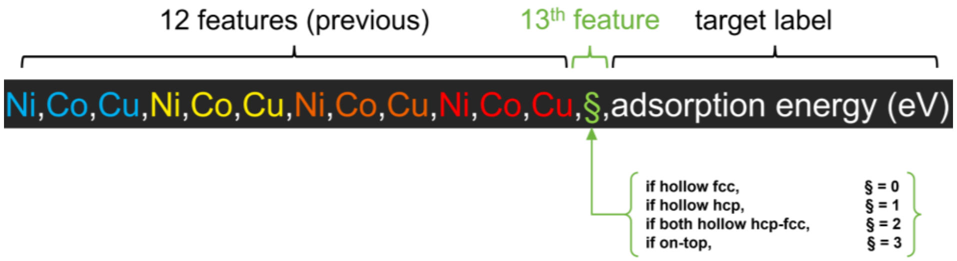

Figure 3.6: Introduced 13th feature (§) on merging the four datasets into one as a description of type of site among fcc, hcp, hcp-fcc and on-top.

After training and testing with this four times increased data set, followed by model optimization with hyperparameter tuning, we found an optimized XGBR model with the least Test RMSE of 0.1072 eV (Figure 3.7) among all the considered ML models. The optimized values of hyperparameters for this model have been described in the appendix - A (Table A2). To verify the RMSE and performance of this XGBR model, we computed and compared DFT adsorption energies of randomly selected 4 catalysts with ML1 and ML2 methods. As it can be evidently observed from the Table 3.1 that the new model was able to predict more closely with the DFT results in case of hcp-fcc sites adsorption energies. Hence, this new model was chosen to substitute the previous SVR model for the better-predicted adsorption energies results of 2 H^* at hcp-fcc sites. The respective final well-optimized algorithms were fed with 63 adsorption energies with their corresponding feature sets, and the prediction of complete 5400 microstructures was performed for hcp, fcc, hcp with fcc, and on-top data sets.

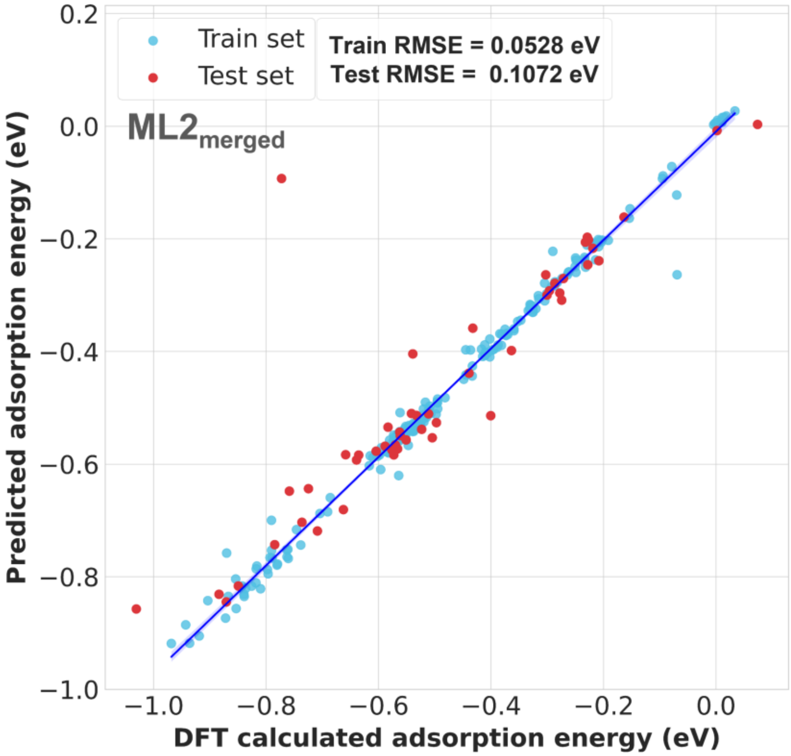

Figure 3.7: Plot of DFT calculated adsorption energies (ΔE_{calc}) versus predicted adsorption energies (ΔE_{pred}) with its indicated test and train RMSE values for merged four datasets with optimized XGBR model. ML2 represents the method 2 by considering merged datasets.

Table 3.1: Comparison table with ML1 (individual $ML1_{hcp}$, $ML1_{fcc}$, $ML1_{hcp\text{-}fcc}$, and $ML1_{on\text{-}top}$), ML2 (merged) and the DFT calculated adsorption energies of 4 selected electrocatalysts.

Alloy system (microstructures)	**Method**	**Adsorption energy (eV)**			
		hcp	**fcc**	**hcp-fcc**	**on-top**
1,1,0,0,0,2,3,0,1,0,3,0	ML1	-0.45	-0.47	-0.80	-0.30
	ML2	-0.46	-0.47	-0.67	-0.31
	DFT	**-0.45**	**-0.47**	**-0.51**	**-0.29**
1,0,1,0,0,2,4,0,0,0,0,3	ML1	-0.43	-0.47	-0.80	-0.36
	ML2	-0.45	-0.49	-0.90	-0.35
	DFT	**-0.42**	**-0.45**	**-1.05**	**-0.36**

0,2,0,0,0,2,3,1,0,1,1,1	ML1	-0.46	-0.45	-0.80	-0.35
	ML2	-0.45	-0.45	-0.66	-0.30
	DFT	**-0.47**	**-0.48**	**-0.56**	**-0.36**
0,2,0,0,0,2,3,0,1,0,2,1	ML1	-0.46	-0.45	-0.80	-0.36
	ML2	-0.44	-0.45	-0.68	-0.30
	DFT	**-0.44**	**-0.48**	**-0.54**	**-0.33**

3.4. Feature Importance

The features are mainly responsible for any predictions, possessing different capturing percentages. The permutation_importance module has been employed, as implemented in the scikit-learn library, *[36]* to figure out their respective contributions during the prediction. As shown in the Figure 3.8a, region 1 has a relatively more significant influence than other regions. Whereas Cu, present in region 1 (Cu_{r_1}), has a maximum influence when predicting adsorption energies by ML1 models for all four sites, especially at the on-top sites. In the second ML method (Figure 3.8b), we observed a similar trend among the features for the microstructure model, along with the highest scoring value of the 13th feature due to a substantial shift from one site environment to other.

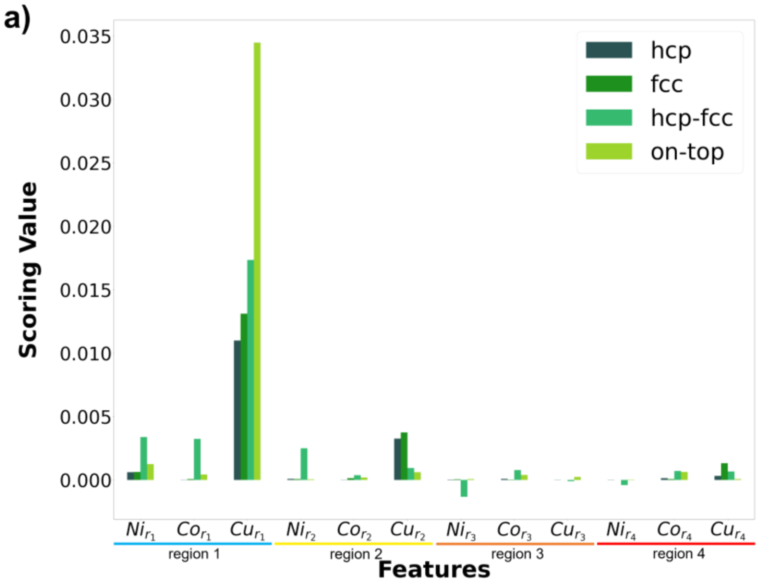

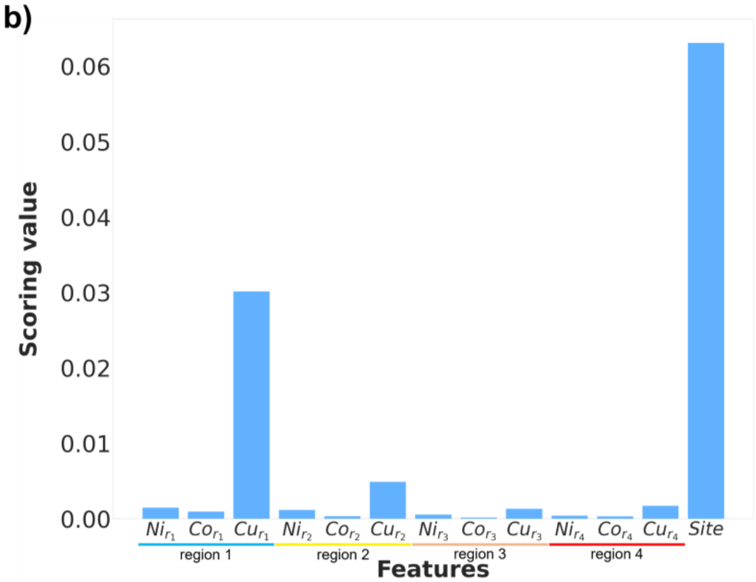

Figure 3.8: Representation of feature importance by scoring values (negative mean squared error) against a) 12 features in individual ML1 models by method 1 ($ML1_{hcp}$, $ML1_{fcc}$, $ML1_{hcp\text{-}fcc}$, and $ML1_{on\text{-}top}$), and b) 13 features in ML2 model by method 2 (by merging all the four datasets). Metal-wise subscripted r_1, r_2, r_3, and r_4 indicate region 1, 2, 3, and 4 of the microstructure, respectively.

After obtaining predicted adsorption energies of the complete 5400 combinations for all four datasets, we screened them to select the most active catalyst (microstructures).

3.5. Catalyst Screening

Given that Pt is the currently available benchmark catalyst for the HER, we have considered the adsorption energy of HER intermediates on Pt as our screening criteria using equation 3.2 (where $\Delta E_{H^*}^{Pt}$ is the H^* adsorption energy with pure Pt catalyst, and $\Delta E_{H^*}^{x}$ is the H^*adsorption energy with taken alloy catalyst x) condition over 5400 adsorption energy values. The range for screening criteria was taken as $\Delta E_{H^*}^{Pt} \pm 0.15$ and the range was set for further studies after receiving an adequate number of catalysts through it.

$$\left[\Delta E_{H^*}^{Pt} - 0.15\ eV\right] < \Delta E_{H^*}^{x} < \left[\Delta E_{H^*}^{Pt} + 0.15\ eV\right] \qquad (3.2)$$

For this, we used the same DFT tool (GPAW) and computational conditions on a pure Pt fcc(111) slab of 64 atoms (4×4×4) with its considered lattice parameter (Table A1). Initially, the same counterpart Pt sites were considered for the DFT results as references. However, the final sites were H^* at hollow hcp, H^* at hollow fcc, $2H^*$ coverage at hollow fcc-fcc, and H_2^* at hollow fcc (Figure 3.9). The respective adsorption preference of $2H^*$ coverage and H_2^* were in agreement with the previously reported studies. *[61-63]* The DFT computed results for Pt(111) are given in appendix – A (Table A3).

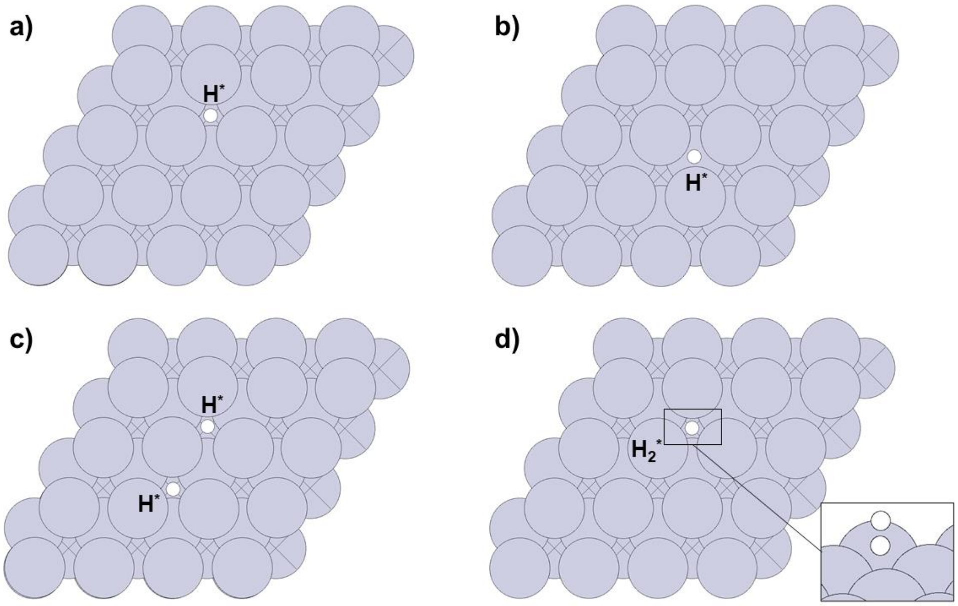

Figure 3.9: Considered four cases of adsorption at 4 × 4 × 4 periodic Pt fcc(111) slab as a reference for the screening: a) H^* at hollow fcc, b) H^* at hollow hcp, c) $2H^*$ at hollow fcc-fcc, and d) H_2^* at fcc hollow site.

As represented by the screening flow chart in Figure 3.10, after collecting 5400 predicted results of site wise datasets (step 1) and imposing the equation 4 screening criteria on each 5400 sets with their pure Pt counterparts (step 2), we obtained 4768 microstructures from hcp, 5094 microstructures from fcc, 3084 microstructures from hcp-fcc, and 900 microstructures from on-top sites. In the end, 27 common (C) microstructures were selected among hcp, fcc, hcp-fcc, and on-top sets (step 3).

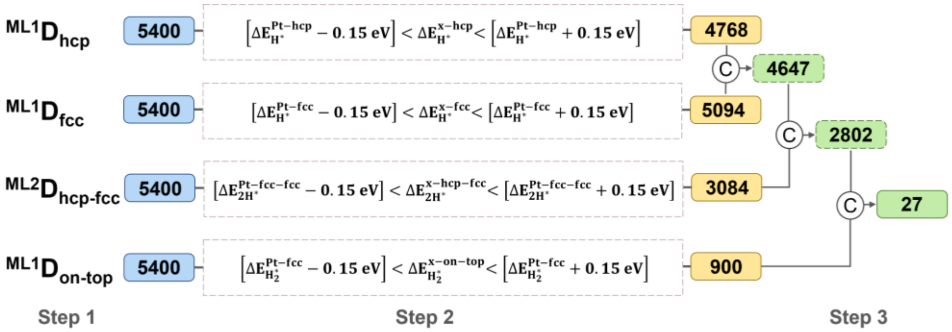

Figure 3.10: Flowchart of the performed screening and selection procedure. D_{hcp}, D_{fcc}, $D_{on\text{-}top}$ datasets of 5400 were predicted by ML1 methods, and $D_{hcp\text{-}fcc}$ dataset was predicted by ML2 method.

These 27 structures are the most active electrocatalysts, comprising 4 bimetallic and 23 trimetallic microstructures. Predicted adsorption energies of the selected 27 catalyst and their microstructure compositions have been provided in the appendix - A (Table A4 and Table A5). All 4 bimetallic catalysts obtained comprise of Ni and Cu only, validating the already reported computational and experimental studies *[64, 65]* on CuNi bimetallic surface alloy for H_2O adsorption and dissociation. Also, the expected synergistic effect between all three metal with optimum combinations in trimetallic surfaces were observed to have better results. Region 1 has been occupied by the two Cu atoms in all 27 catalysts, underlying its significant contribution during H_2^* desorption, whereas region 2 has no Cu atoms throughout the selected 27, supporting the fact that Ni or Co atom's presence would aid H^* adsorption effectively at hollow hcp and fcc sites. This observation is also in agreement with performed feature importance analysis.

3.5.1. Catalyst Stability

To examine the thermodynamic stability of our selected alloy catalyst compositions, we have calculated the formation energies of 10 catalysts. These 10 catalysts have been randomly selected from the finally obtained 27 catalysts, which includes 2 bimetallic and 8 trimetallic combinations. Formation energies of considered 10 catalysts were calculated using the following equation:

$$E_{form} = (E_{cat} - xE_{bulk}^{Ni} - yE_{bulk}^{Co} - zE_{bulk}^{Cu})/N \qquad (3.3)$$

Where, E_{form} represents the formation energy per atom of the considered catalyst, E_{cat} represents the total energy of the considered optimized catalyst structure. x, y, and z are the respective numbers of Ni, Co, and Cu atoms in a cell of $Ni_xCo_yCu_z$ alloy. E_{bulk}^{Ni}, E_{bulk}^{Co}, and E_{bulk}^{Cu} are the total energies of bulk fcc Ni, hcp Co, and fcc Cu per atom, respectively. N (N = 64) is the total number of atoms present in the slab system. The appendix - A (Text A2 and Table A6) has the details of computed formation energies. The DFT calculated formation energies of all the 10 catalytic systems show that they can be synthesized as such positive formation energies of various surface alloy systems are reported to be stable. *[66-70]*

3.5.2. Catalyst Activity

In HER, an ideal catalyst should have nearly zero Gibbs free energy. *[71]* To further ascertain our results, the free energy (ΔG_{H^*}) for the Pt (111) and 3 selected catalysts (Figure 3.11) among the same 10 catalysts have been calculated. We performed the free energy analysis with the computed results of the four catalysts (Pt(111), catalyst 1, catalyst 2 and catalyst 3) to observe their activity during the HER (Text A3 and Table A7 in appendix - A). The two of most stable catalysts (Catalyst 1: 002200400120 and Catalyst 2: 002200211120) have been considered after observing their least formation energy values among the 8 trimetallic combination catalysts. Furthermore, one bimetallic catalyst (Catalyst 3: 002200202201) has also been considered to examine bimetallic specie's activity during the HER as well. The following equation was employed for free energy calculation.

$$\Delta G = \Delta E + \Delta ZPE - T\Delta S \tag{3.4}$$

Here, ΔE is the total energy of the optimized system, ΔZPE represents the change in the zero-point energy (ZPE), T represents the temperature, and ΔS is the change in the entropy of the reaction. However, $T\Delta S$ term is insignificant to the ΔG value by considering T as 0 K. The ZPE is obtained from the calculated vibrational frequencies (ν_i) resulted from the density functional perturbation (DFPT) method.

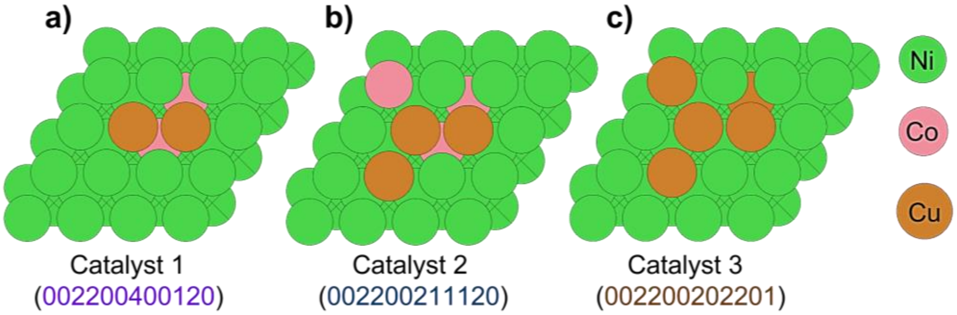

Figure 3.11: Three selected catalyst for free energy calculation. a) catalyst 1 ($Ni_{60}Co_2Cu_2$) and b) catalyst 2 ($Ni_{58}Co_3Cu_3$) are trimetallic, whereas c) catalyst 3 ($Ni_{59}Co_0Cu_5$) is a bimetallic combination.

The change in free energies (ΔG_{H^*}) for Pt(111), catalyst 1, catalyst 2, and catalyst 3 were found to be -0.20 eV, -0.14 eV, -0.10 eV, and -0.17 eV (Figure 3.12a). The (ΔG_{H^*}) of the three selected catalysts (catalyst 1, 2, and 3) were found close to 0 eV, while Pt(111) has been taken as a reference catalyst, suggesting that a synergistic effect between Ni, Co, and Cu is able to provide a better activity for the HER. From the free energy changes of the overall reaction considering all four catalytic systems, we found step 3 as the potential determining step (PDS) (Figure 3.12b). Moreover, both the catalyst (catalyst 1 and 2) requires lower applied potential than Pt catalyst. However, the trimetallic catalyst requires lowest applied potential among all three. The second step (H^* + H^*) analysis showed that the coverage efficiency of the selected catalysts is better than the Pt(111) surface. In the final step (H_2^*), it also fulfilled the criteria of an ideal catalyst having weak binding with the H_2 molecule, to provide a smooth desorption from the surface.

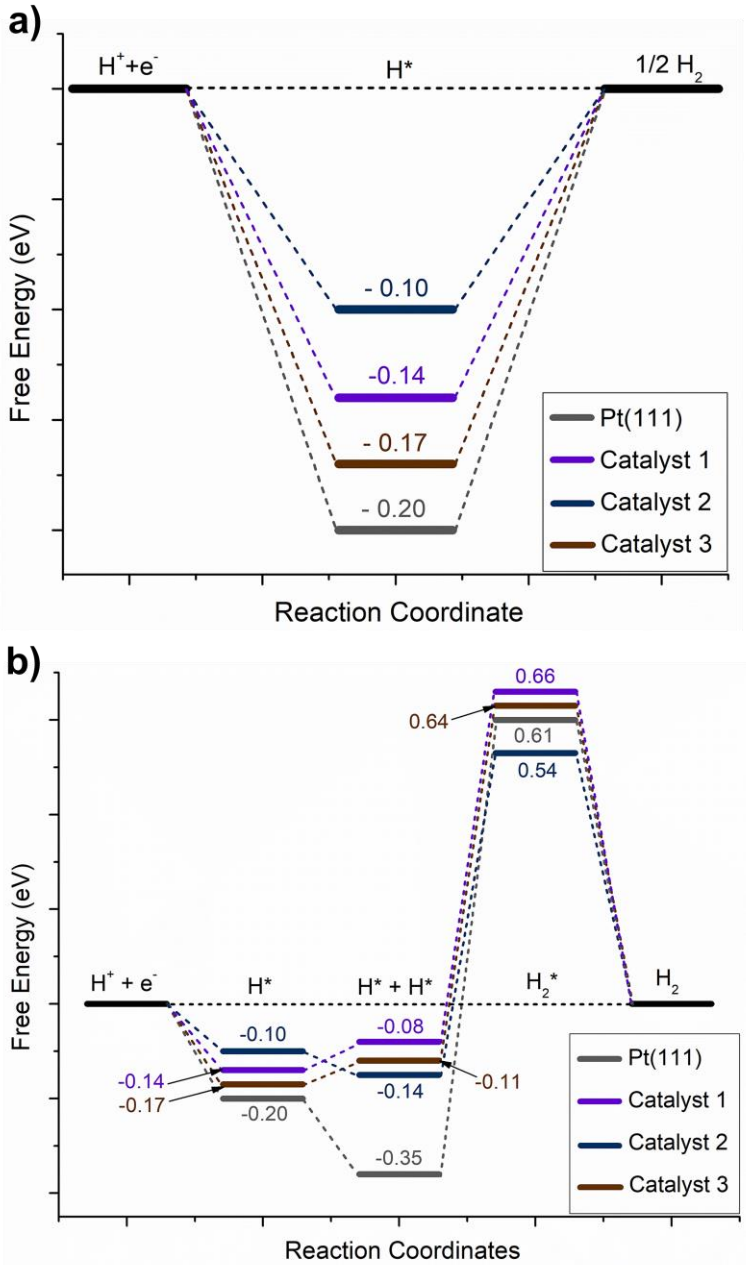

Figure 3.12: Gibbs free energy change during HER on Pt(111), catalyst 1 ($Ni_{60}Co_2Cu_2$), catalyst 2 ($Ni_{58}Co_3Cu_3$), and catalyst 3 ($Ni_{59}Co_0Cu_5$) surfaces for the a) H adsorption step and b) complete HER.

CHAPTER 4

4. Conclusions

We have presented a method to obtain active NiCoCu-based catalysts for the HER using microstructure modeling, DFT tool, and supervised ML models. A comprehensive microstructure model was designed to study the adsorbate coverage effect and feature generation for ML. We have selected 63 combinations among 5400 catalysts for the DFT calculations to train the ML models. The XGBR models were able to predict adsorption energies most accurately in respective individual datasets. Nevertheless, we improved prediction accuracy for one of the encountered less accurate models with the help of label encoding technique over the merged dataset. Then, the DFT results of Pt were taken as reference data to perform catalysts screening. The screened 27 cost-efficient active catalysts have the potential to provide an optimum catalytic surface for the HER and can be an alternative to high-cost PGM-based catalysts. Furthermore, we calculated formation energy values of the considered 10 catalysts and found that they are stable. With the performed free energy analysis, the trimetallic catalysts were found to be more favorable for the HER than bimetallic catalysts. In this way, the discovery of such heterogeneous catalysts could be accelerated dramatically by performing minimal DFT and employing intelligent ML algorithms. The suggested method is envisioned to provide a leap forward in designing several other heterogeneous catalysts in a small timeframe.

APPENDIX - A

Supporting Information

I. Lattice parameters

Table A1. Fcc lattice parameters (a) used for our DFT calculations.

Metal	**a (Å)**
Ni	3.53
Pt	3.91

II. Microstructure combinations

Text A1. Following expression has been employed to calculate the total number of designed microstructure combinations with replacement:

$$C^{R}_{(n,r)} = \frac{(r+n\ -1)!}{r!\,(n-1)!}$$

Here,

n = number of possible sites present in a region

r = maximum possible number of metals that can be placed in the region (among Ni/Co/Cu)

All possible combinations within region 1, $r_1 = \frac{(2+3\ -1)!}{2!(3-1)!}$ = 6

All possible combinations within region 2, $r_2 = \frac{(2+3\ -1)!}{2!(3-1)!}$ = 6

All possible combinations within region 3, $r_3 = \frac{(4+3-1)!}{4!(3-1)!} = 15$

All possible combinations within region 4, $r_4 = \frac{(3+3-1)!}{3!(3-1)!} = 10$

Total number of combinations including all four regions,

$$r_1 \times r_2 \times r_3 \times r_4 = 5400$$

III. Hyperparameter tunning for machine learning

Table A2: Optimization of hyperparameters with their corresponding RMSE values in each dataset for the 5 considered regression models for considered ML methods (M).

M	**ML models**	**Optimized hyperparameters**	**RMSE (eV)**
(ML1) Hollow hcp	Linear	copy_X = False, fit_intercept = False, n_jobs = 34, normalize = ‘deprecated’, positive=’False’	0.0310
	KRR	alpha = 1, coef0 = 1, degree = 3, gamma = None, kernel = ‘linear’, kernel_params = None	0.0315
	SVR	C = 10, coef0 = 1.0, degree = 3, epsilon = 0.0, gamma = ‘scale’, kernel = ‘rbf’, max_iter = -1, tol = 0.001	0.0343
	XGBR	base_score = 0.75, booster = ‘gbtree’, cv = 5, learning_rate = 0.05, max_depth = 2, min_child_weight = 1, n_estimators = 1100, verbose = 4	0.0151
	GPR (RBF)	alpha = 0.001, kernel__k1__k1__constant_value = 1.0,	0.0328

		kernel__k1__k2__length_scale = 2.05, kernel__k2__noise_level = 1.0	
(ML1) Hollow fcc	Linear	copy_X = True, fit_intercept = True, n_jobs = None, normalize = ‘deprecated’, positive = False	0.0302
	KRR	alpha = 1, coef0 = 1, degree = 3, gamma = None, kernel = ‘linear’, kernel_params = None	0.0334
	SVR	C = 5.0, coef0 = 2.0, degree = 2, epsilon = 0.0, gamma = ‘auto’, kernel = ‘poly’, max_iter = 2, tol = 0.01	0.0477
	XGBR	base_score = 0.75, booster = ‘gbtree’, cv = 5, learning_rate = 0.05, max_depth = 2, min_child_weight = 1, n_estimators =1100, verbose = 4	0.0108
	GPR (RBF)	alpha = 1e-10, kernel__k1__k1__constant_value = 10.0, kernel__k1__k2__length_scale = 5.0, kernel__k2__noise_level = 2.0	0.0334
(ML1) Hollow hcp-fcc	Linear	copy_X = False, fit_intercept = False, n_jobs = 1, normalize = ‘deprecated’, positive = True	0.2709
	KRR	alpha = 1, coef0 = 1, degree = 4, gamma = 0.2, kernel = ‘linear’, kernel_params = None	0.2699
	SVR	C = 1.0, coef0 = 4.0, epsilon = 0.3, gamma = ‘auto’, kernel = ‘linear’, tol = 0.01	0.2584
	XGBR	base_score = 0.8, booster = ‘gbtree’, cv = 4, learning_rate = 0.1, max_depth = 3, min_child_weight = 1.5, n_estimators = 600, verbose = 2	0.2833

	GPR (RBF)	alpha = 1e-10, kernel__k1__k1__constant_value = 4.95, kernel__k1__k2__length_scale = 10.05, kernel__k2__noise_level = 1.0	0.2641
(ML1) On-top	Linear	copy_X = True, fit_intercept = True, n_jobs = 44, normalize = ‘deprecated’, positive = True	0.0606
	KRR	alpha = 0.09, coef0 = -1.5, degree = 3.0, gamma = 0.1, kernel = ‘laplacian’, kernel_params = None	0.0559
	SVR	C = 1.0, coef0 = 4.0, degree = 2, epsilon = 0.1, gamma = ‘scale’, kernel = ‘sigmoid’, max_iter = 2, tol = 0.01	0.0770
	XGBR	base_score = 0.80, booster = ‘gbtree’, cv = 5, learning_rate = 0.2, max_depth = 3, min_child_weight = 1.5, n_estimators = 600, verbose = 2	0.0244
	GPR (RBF)	alpha = 1e-05, kernel__k1__k1__constant_value = 5.05, kernel__k1__k2__length_scale = 2.05, kernel__k2__noise_level = 1.95	0.0611
(ML2) Merged	Linear	copy_X = True, fit_intercept = True, n_jobs = None, normalize = ‘deprecated’, positive = False	0.2089
	KRR	alpha = 49.1, coef0 = 5.5, degree = 2.0, gamma = 1.1, kernel = ‘polynomial’	0.1854
	SVR	C = 5.0, coef0 = 2.0, degree = 2, epsilon = 0.3, gamma = ‘scale’, kernel = ‘linear’, max_iter = -1, tol = 0.002	0.2027
	XGBR	base_score = 0.25, booster = ‘gbtree’, cv = 3, learning_rate = 0.05, max_depth = 15,	0.1072

	min_child_weight = 2, n_estimators = 100, verbose = 2	
GPR (RBF)	alpha = 0.001, kernel__k1__k1__constant_value = 4.95, kernel__k1__k2__length_scale = 5.05, kernel__k2__noise_level = 10.05	0.2069

IV. Pt(111) catalyst for the reference

Table A3. DFT calculated adsorption energies of adsorbate(s) on the considered Pt(111) sites.

Pt(111) site	**Adsorption energy (eV)**
H^* at hollow hcp	-0.41
H^* at hollow fcc	-0.47
2 H^* at hollow fcc-fcc	-0.92
H_2^* at hollow fcc	0.00

V. Selected 27 catalysts

Table A4. Predicted adsorption energies from respective ML methods (ML1, and ML2) of finally selected 27 catalysts with their microstructure features and composition type.

Sl. No.	**Microstructure**	**Type$^{\#}$**	**Predicted adsorption energy (eV)**			
			ML1$_{hcp}$	**ML1$_{fcc}$**	**ML2$_{hcp\text{-}fcc}$**	**ML1$_{on\text{-}top}$**
1	002200400120	tm	-0.38	-0.36	-0.77	0.00
2	002200310300	tm	-0.38	-0.38	-0.77	-0.01
3	002200310210	tm	-0.38	-0.38	-0.77	-0.02
4	002200310120	tm	-0.38	-0.36	-0.80	0.00
5	002200301300	bm	-0.38	-0.38	-0.83	-0.03
6	002200301210	tm	-0.38	-0.38	-0.83	-0.03

7	002200301201	bm	-0.38	-0.41	-0.79	-0.03
8	002200301120	tm	-0.37	-0.36	-0.83	0.00
9	002200301111	tm	-0.38	-0.41	-0.79	-0.02
10	002200301030	tm	-0.36	-0.36	-0.80	0.02
11	002200301021	tm	-0.37	-0.39	-0.78	0.01
12	002200220120	tm	-0.39	-0.37	-0.79	0.00
13	002200211300	tm	-0.38	-0.38	-0.82	-0.02
14	002200211210	tm	-0.38	-0.38	-0.82	-0.03
15	002200211201	tm	-0.39	-0.41	-0.78	-0.02
16	002200211120	tm	-0.38	-0.36	-0.82	0.00
17	002200211111	tm	-0.39	-0.41	-0.78	-0.02
18	002200211030	tm	-0.37	-0.36	-0.79	0.03
19	002200211021	tm	-0.38	-0.40	-0.77	0.01
20	002200202300	bm	-0.38	-0.38	-0.81	0.01
21	002200202210	tm	-0.38	-0.38	-0.81	0.00
22	002200202201	bm	-0.38	-0.41	-0.77	0.01
23	002200202120	tm	-0.38	-0.36	-0.81	0.03
24	002200202111	tm	-0.38	-0.41	-0.77	0.01
25	002200202030	tm	-0.37	-0.36	-0.79	0.06
26	002110301030	tm	-0.33	-0.36	-0.79	0.00
27	002020301030	tm	-0.34	-0.34	-0.78	0.01

[#] **Composition type of microstructure:** bm = bimetallic, tm = trimetallic

Table A5. Microstructure composition formula of finally selected 27 catalysts with their corresponding region-wise 12 features.

Sl. No.	**Formula**	**Features[‡]**											
		region 1			**region 2**			**region 3**			**region 4**		
		Ni_{r_1}	Co_{r_1}	Cu_{r_1}	Ni_{r_2}	Co_{r_2}	Cu_{r_2}	Ni_{r_3}	Co_{r_3}	Cu_{r_3}	Ni_{r_4}	Co_{r_4}	Cu_{r_4}
1	$Ni_7Co_2Cu_2$	0	0	2	2	0	0	4	0	0	1	2	0
2	$Ni_8Co_1Cu_1$	0	0	2	2	0	0	3	1	0	3	0	0

3	$Ni_7Co_2Cu_2$	0	0	2	2	0	0	3	1	0	2	1	0
4	$Ni_6Co_3Cu_2$	0	0	2	2	0	0	3	1	0	1	2	0
5	$Ni_8Co_0Cu_3$	0	0	2	2	0	0	3	0	1	3	0	0
6	$Ni_7Co_1Cu_3$	0	0	2	2	0	0	3	0	1	2	1	0
7	$Ni_7Co_0Cu_4$	0	0	2	2	0	0	3	0	1	2	0	1
8	$Ni_6Co_2Cu_3$	0	0	2	2	0	0	3	0	1	1	2	0
9	$Ni_6Co_1Cu_4$	0	0	2	2	0	0	3	0	1	1	1	1
10	$Ni_5Co_3Cu_3$	0	0	2	2	0	0	3	0	1	0	3	0
11	$Ni_5Co_2Cu_4$	0	0	2	2	0	0	3	0	1	0	2	1
12	$Ni_5Co_4Cu_2$	0	0	2	2	0	0	2	2	0	1	2	0
13	$Ni_7Co_1Cu_3$	0	0	2	2	0	0	2	1	1	3	0	0
14	$Ni_6Co_2Cu_3$	0	0	2	2	0	0	2	1	1	2	1	0
15	$Ni_6Co_1Cu_4$	0	0	2	2	0	0	2	1	1	2	0	1
16	$Ni_5Co_3Cu_3$	0	0	2	2	0	0	2	1	1	1	2	0
17	$Ni_5Co_2Cu_4$	0	0	2	2	0	0	2	1	1	1	1	1
18	$Ni_4Co_4Cu_3$	0	0	2	2	0	0	2	1	1	0	3	0
19	$Ni_4Co_3Cu_4$	0	0	2	2	0	0	2	1	1	0	2	1
20	$Ni_7Co_0Cu_4$	0	0	2	2	0	0	2	0	2	3	0	0
21	$Ni_6Co_1Cu_4$	0	0	2	2	0	0	2	0	2	2	1	0
22	$Ni_6Co_0Cu_5$	0	0	2	2	0	0	2	0	2	2	0	1
23	$Ni_5Co_2Cu_4$	0	0	2	2	0	0	2	0	2	1	2	0
24	$Ni_5Co_1Cu_5$	0	0	2	2	0	0	2	0	2	1	1	1
25	$Ni_4Co_3Cu_4$	0	0	2	2	0	0	2	0	2	0	3	0
26	$Ni_4Co_4Cu_3$	0	0	2	1	1	0	3	0	1	0	3	0
27	$Ni_3Co_5Cu_3$	0	0	2	0	2	0	3	0	1	0	3	0

[‡] **Features:** Number of indicated metal atoms in indicated regions

VI. Formation energy

Text A2. The DFT computed energies of single atoms from the bulk of Ni, Co, and Cu are: E_{bulk}^{Ni} = -7.20 eV, E_{bulk}^{Co} = -7.73 eV, and E_{bulk}^{Cu} = -3.54 eV.

Table A6. Calculated total ($T_{catalyst}$) and formation (E_{form}) energy of considered 10 catalysts among the screened in 27 with their corresponding microstructures.

Sl. no.	**Microstructure**	**Type**	**Catalyst**$^{\alpha}$	**$T_{catalyst}$ (eV)**	**E_{form} (eV/atom)**
1	002200400120	tm	$Ni_{60}Co_2Cu_2$	-437.10	0.27
2	002200301201	bm	$Ni_{60}Co_0Cu_4$	-428.14	0.28
3	002200301111	tm	$Ni_{59}Co_1Cu_4$	-428.84	0.27
4	002200220120	tm	$Ni_{58}Co_4Cu_2$	-438.30	0.27
5	002200211201	tm	$Ni_{59}Co_1Cu_4$	-428.75	0.28
6	002200211120	tm	$Ni_{58}Co_3Cu_3$	-434.09	0.27
7	002200211111	tm	$Ni_{58}Co_2Cu_4$	-429.45	0.27
8	002200211021	tm	$Ni_{57}Co_3Cu_4$	-430.19	0.27
9	002200202201	bm	$Ni_{59}Co_0Cu_5$	-424.56	0.28
10	002200202111	tm	$Ni_{58}Co_1Cu_5$	-425.25	0.27

$^{\alpha}$**Catalyst composition formula:**

Base (Ni_{53}) + Microstructure ($Ni_xCo_yCu_z$) = Catalyst ($Ni_{53+x}Co_yCu_z$)

Here,

$x + y + z = 11$ (11 atoms from all four regions of the microstructure)

VII. Free energy analysis

Text A3. Following are the calculated total energies of Pt(111) and three selected catalysts:

a) Pt(111) = -391.01 eV
b) Catalyst 1 = -437.10 eV
c) Catalyst 2 = -434.09 eV
d) Catalyst 3 = -424.56 eV

Table A7. Calculated total energy, ZPE corrections and free energy with considered adsorbates at Pt(111) and three selected active catalysts for HER. All the values below in the table are in eV.

	Adsorbate with site	**$T_{catalyst}$**	**ZPE corrections**	**Free Energy**
Pt(111)	H^* at hollow hcp	-394.73	0.14	-394.59
	H^* at hollow fcc	-394.83	0.16	-394.67
	2 H^* at hollow fcc-fcc	-398.63	0.36	-398.27
	H_2^* at hollow hcp	-397.71	0.40	-397.31
Catalyst 1	H^* at hollow hcp	-440.82	0.14	-440.69
	H^* at hollow fcc	-440.82	0.14	-440.67
	2 H^* at hollow hcp-fcc	-444.37	0.29	-444.08
	H_2^* at on-top	-443.81	0.46	-443.35
Catalyst 2	H^* at hollow hcp	-437.85	0.19	-437.65
	H^* at hollow fcc	-437.82	0.17	-437.64
	2 H^* at hollow hcp-fcc	-441.40	0.24	-441.16
	H_2^* at on-top	-440.82	0.34	-440.47
Catalyst 3	H^* at hollow hcp	-428.28	0.13	-428.14
	H^* at hollow fcc	-428.31	0.12	-428.19
	2 H^* at hollow hcp-fcc	-431.86	0.28	-431.59
	H_2^* at on-top	-431.25	0.42	-430.84

REFERENCES

[1] REN21; Renewables 2021 Global Status Report, https://www.ren21.net/reports/global-status-report/

[2] J. Bard, R. Parsons and J. Jordan (Eds), Standard Potentials in Aqueous Solutions; A Marcel Dekker, New York, p. 51, 1985 (ISBN: 9780824772918)

[3] Sabatier, P. Hydrogénations et Déshydrogénations par Catalyse. Ber. Dtsch. Chem. Ges. 1911, 44, 1984–2001 (DOI: 10.1002/cber.19110440303)

[4] Bligaard, T.; Norskov, J. K.; Dahl, S.; Matthiesen, J.; Christensen, C. H.; Sehested, J. The Brønsted-Evans-Polanyi Relation and the Volcano Curve in Heterogeneous Catalysis. J. Catal. 2004, 224, 206−217 (DOI: 10.1016/j.jcat. 2004.01.026)

[5] Nørskov, J. K.; Bligaard, T.; Logadottir, A.; Kitchin, J. R.; Chen, J. G.; Pandelov, S.; Stimming, U. Trends in the Exchange Current for Hydrogen Evolution. J. Electrochem. Soc. 2005, 152, J23–J26 (DOI: 10.1149/1.1856988)

[6] Hosoya, Y. & Fujii, Y. Analysis of Energy Strategies to Halve CO_2 Emissions by the Year 2050 with a Regionally Disaggregated World Energy Model. Energy Procedia 2011, 4, 5853–5860 (DOI: 10.1016/j.egypro.2011.02.584)

[7] Li, C.; Baek, J.-B. Recent Advances in Noble Metal (Pt, Ru, and Ir)-Based Electrocatalysts for Efficient Hydrogen Evolution Reaction. ACS Omega 2020, 5, 31–40 (DOI: 10.1021/acsomega.9b03550)

[8] Li, M.; Duanmu, K.; Wan, C.; Cheng, T.; Zhang, L.; Dai, S.; Chen, W.; Zhao, Z.; Li, P.; Fei, H.; Zhu, Y.; Yu, R.; Luo, J.; Zang, K.; Lin, Z.; Ding, M.; Huang, J.; Sun, H.; Guo, J.; Pan, X.; Goddard, W. A., III; Sautet, P.; Huang, Y.; Duan, X. Single-atom Tailoring of

Platinum Nanocatalysts for High-Performance Multifunctional Electrocatalysis. Nat. Catal. 2019, 2, 495–503 (DOI: 10.1038/s41929-019-0279-6)

[9] Paul, R.; Zhu, L.; Chen, H.; Qu, J.; Dai, L. Recent Advances in Carbon-based Metal-free Electrocatalysts. Adv. Mater . 2019, 31, 1806403–1806427 (DOI: 10.1002/adma. 201806403)

[10] Kong, D.; Cha, J. J.; Wang, H.; Lee, H. R.; Cui, Y. First-row Transition Metal Dichalcogenide Catalysts for Hydrogen Evolution Reaction. Energy Environ. Sci. 2013, 6, 3553–3558 (DOI: 10.1039/C3EE42413H)

[11] Popczun, E. J.; Mckone, J. R.; Read, C. G.; Biacchi, A. J.; Wiltroult, A. M.; Lewis, N. S.; Schaak, R. E. Nanostructured Nickel Phosphide as an Electrocatalyst for the Hydrogen Evolution Reaction. J. Am. Chem. Soc. 2013, 135, 9267–9270 (DOI: 10.1021/ja403440e)

[12] Mujtaba, J.; He, L.; Zhu, H.; Xiao, Z.; Huang, G.; Solovev, A. A.; Mei, Y. Co_9S_8 Nanoparticles for Hydrogen Evolution. ACS Appl. Nano Mater. 2021, 4, 1776–1785 (DOI: 10.1021/acsanm.0c03171)

[13] Chen, W. F.; Sasaki, K.; Ma, C.; Frenkel, A. I.; Marinkovic, N.; Muckerman, J. T.; Zhu, Y.; Adzic, R. R. Hydrogen-evolution Catalysts Based on Non-Noble Metal Nickel-Molybdenum Nitride Nanosheets. Angew. Chem., Int. Ed. 2012, 51, 6131–6135 (DOI: 10.1002/anie.201200699)

[14] Miles, M. H.; Thomason, M. A. Periodic Variations of Over Voltages for Water Electrolysis in Acid Solutions from Cyclic Voltammetric Studies. J. Electrochem. Soc. 1976, 123, 1459−1461 (DOI: 10.1149/1.2132619)

[15] Zhu, J.; Hu, L.; Zhao, P.; Lee, L. Y. S.; Wong, K.-Y. Recent Advances in Electrocatalytic Hydrogen Evolution Using Nanoparticles. Chem. Rev. 2020, 120, 851– 918 (DOI: 10.1021/acs.chemrev.9b00248)

[16] Vij, V.; Sultan, S.; Harzandi, A. M.; Meena, A.; Tiwari, J. N.; Lee, W. G.; Yoon, T.; Kim, K. S. Nickel-Based Electrocatalysts for Energy-

Related Applications: Oxygen Reduction, Oxygen Evolution, and Hydrogen Evolution Reactions. ACS Catal. 2017, 7, 7196–7225 (DOI: 10.1021/acscatal.7b01800)

[17] Zou, X.; Huang, X.; Goswami, A.; Silva, R.; Sathe, B. R.; Mikmeková, E.; Asefa, T. Cobalt- Embedded Nitrogen-Rich Carbon Nanotubes Efficiently Catalyze Hydrogen Evolution Reaction at All pH Values. Angew. Chem., Int. Ed. 2014, 126, 4461−4465 (DOI: 10.1002/ange.201311111)

[18] Deng, J.; Ren, P.; Deng, D.; Bao, X. Enhanced Electron Penetration through an Ultrathin Graphene Layer for Highly Efficient Catalysis of the Hydrogen Evolution Reaction. Angew. Chem., Int. Ed. 2015, 54, 2100−2104 (DOI: 10.1002/anie.201409524)

[19] Kim, H.; Park, H.; Oh, S.; Kim, S. K. Facile Electrochemical Preparation of Nonprecious Co-Cu Alloy Catalysts for Hydrogen Production in Proton Exchange Membrane Water Electrolysis. Int. J. Energy Res. 2020, 44, 2833−2844 (DOI: 10.1002/er.5099)

[20] Schwarz, M.; Faisal, F.; Mohr, S.; Hohner, C.; Werner, K.; Xu, T.; Skála, T.; Tsud, N.; Prince, K. C.; Matolín, V.; Lykhach, Y.; Libuda, J. Structure-Dependent Dissociation of Water on Cobalt Oxide. J. Phys. Chem. Lett. 2018, 9, 2763–2769 (DOI: 10.1021/ acs.jpclett.8b01033)

[21] Wang, J.; Liu, Y.; Yang, G. Cobalt Decorated Ultra-Thin Ti_3C_2 MXene Electrocatalyst for High-Efficiency Hydrogen Evolution Reaction. Mater. Res. Express 2019, 6, No. 025056 (DOI: 10.1088/2053-1591/aaf1f0)

[22] Wen, X.; Yang, X.; Li, M.; Bai, L.; Guan, J. Co/CoO_x Nanoparticles Inlaid onto Nitrogen-Doped Carbon-Graphene as a Trifunctional Electrocatalyst. Electrochim. Acta. 2019, 296, 830−841 (DOI: 10.1016/j.electacta.2018.11.129)

[23] Ghosh, S.; Hariharan, S.; Tiwari, A. K. Water Adsorption and Dissociation on Copper/Nickel Bimetallic Surface Alloys: Effect of

Surface Temperature on Reactivity. J. Phys. Chem. C. 2017, 121, 16351–16365 (DOI: 10.1021/acs.jpcc.7b04637)

[24] Wang, T.; Wu, D.; Wang, Y.; Huang, T.; Histand, G.; Wang, T.; Zeng, H. One-Step Solvothermal Fabrication of Cu@PANI Core-Shell Nanospheres for Hydrogen Evolution. Nanoscale. 2018, 10, 22055−22064 (DOI: 10.1039/C8NR06245E)

[25] Shinde, D. V.; Dang, Z.; Petralanda, U.; Palei, M.; Wang, M.; Prato, M.; Cavalli, A.; De Trizio, L.; Manna, L. In Situ Dynamic Nanostructuring of the Cu-Ti Catalyst-Support System Promotes Hydrogen Evolution under Alkaline Conditions. ACS Appl. Mater. Interfaces. 2018, 10, 29583−29592 (DOI: 10.1021/acsami.8b09493)

[26] Gong, X.; Gu, Y.; Zhang, F.; Liu, Z.; Li, Y.; Chen, G.; Wang, B. High-Performance Non-Enzymatic Glucose Sensors Based on CoNiCu Alloy Nanotubes Arrays Prepared by Electrodeposition. Frontiers in Materials. 2019, 6, 3 (DOI: 10.3389/fmats.2019.00003)

[27] Peecher, B. E.; Hampton, J. R. Dealloying Behavior of NiCo and NiCoCu Thin Films, Int. J. Electrochem. 2016, 1−10 (DOI: 10.1155/2016/2935035)

[28] Kuo, Q.; Xinghua, L.; Hong, Z.; Li, W.; Desheng, X.; Haoli, Z.; Baofan, Z.; Nigel, J.M.; Yong, P. Nanoscale Characterization and Magnetic Property of NiCoCu/Cu Multilayer Nanowires. Nanotechnology. 2012, 23, 505707 (DOI: 10.1088/0957-4484/23/50/505707)

[29] Mohsenzadeh, A.; Bolton, K.; Richards, T. DFT Study of the Adsorption and Dissociation of Water on Ni(111), Ni(110) and Ni(100) surfaces. Surface Science. 2014, 627, 1−10 (DOI: 10.1016 /j.susc.2014.04.006)

[30] A. M. Turning, I. Computing Machinery and Intelligence, Mind, LIX, 236, 1950, 433–460, (DOI: 10.1093 /mind/LIX.236.433)

[31] T.A.A. Batchelor, J.K. Pedersen, S.H. Winther, I.E. Castelli, K.W. Jacobsen, J. Rossmeisl High-entropy Alloys as a Discovery Platform for Electrocatalysis. Joule, 2019, 3, 834−845 (DOI: 10.1016/j.joule.2018.12.015)

[32] Pedersen, J. K.; Batchelor, T. A. A.; Bagger, A.; Rossmeisl, J. High-Entropy Alloys as Catalysts for the CO_2 and CO Reduction Reactions. ACS Catal. 2020, 10, 2169–2176 (DOI: 10.1021/acscatal.9b04343)

[33] Roy, D.; Mandal, S. C.; Pathak, B. Machine Learning-Driven High-Throughput Screening of Alloy-Based Catalysts for Selective CO_2 Hydrogenation to Methanol. ACS Appl. Mater. Interfaces. 2021, 13, 47, 56151−56163 (DOI: 10.1021/acsami.1c16696)

[34] Wu, S.; Wang, Z.; Zhang, H.; Cai, J.; Li, J. Deep Learning Accelerates the Discovery of Two-Dimensional Catalysts for Hydrogen Evolution Reaction. Energy Environ. Mater. 2022 (DOI: 10.1002/eem2.12259)

[35] Baghban, A.; Habibzadeh, S.; Zokaee A., F. On the Evaluation of Hydrogen Evolution Reaction Performance of Metal-Nitrogen-Doped Carbon Electrocatalysts using Machine Learning Technique. Sci Rep. 2021, 11, 21911 (DOI: 10.1038/s41598-021-00031-0)

[36] Mao, X.; Wang, L.; Xu, Y.; Wang, P.; Li, Y.; Zhao, J. Computational High-Throughput Screening of Alloy Nanoclusters for Electrocatalytic Hydrogen Evolution. npj Comput. Mater. 2021, 7, 46 (DOI: 10.1038/s41524-021-00514-8)

[37] Pedregosa, F.; Varoquaux, G.; Gramfort, A.; Michel, V.; Thirion, B.; Grisel, O.; Blondel, M.; Prettenhofer, P.; Weiss, R.; Dubourg, V.; Vanderplas, J.; Passos, A.; Cournapeau, D.; Brucher, M.; Perrot, M.; Duchesnay, E. Scikit-learn: Machine Learning in Python. J. Mach. Learn. Res. 2011, 12, 2825−2830 (DOI: 10.48550/arXiv.1201.0490)

[38] Chen, T., & Guestrin, C. XGBoost: A Scalable Tree Boosting System. In Proceedings of the 22nd ACM SIGKDD International Conference on Knowledge Discovery and Data Mining (pp. 785–794). 2016 New York, NY, USA: ACM (DOI: 10.1145/2939672.2939785)

[39] Born M., Oppenheimer J. Zur Quantentheorie der Molekeln, J. Ann. Physik. 1927, 84, 457 (DOI: 10.1002/andp.19273892002)

[40] Hohenberg P., Kohn W. Inhomogeneous Electron gas, Phys. Rev. B, 1964, 136, B864−B871 (DOI: 10.1103/PhysRev. 136.B864)

[41] Kohn W., Sham L.J. Self-Consistent Equations Including Exchange and Correlation Effects, Phys. Rev., 1965, 140, A1133−A1138 (DOI: 10.1103/PhysRev.140.A1133)

[42] Xia B. Y., Wu H.B., Wang X., Lou X.W. Index Facets and Enhanced Electrocatalytic Properties, Angew. Chem. Int. Ed., 2013, 52, 12337−12340 (DOI: 10.1002/anie.201307518)

[43] Martin, R.M. Electronic structure: Basic Theory and Practical Methods, Cambridge University press, 2004 (ISBN: 9780521534406)

[44] Ceperley D.M., Alder B. Ground State of the Electron Gas by a Stochastic Method, J. Phys. Rev. Lett. 1980, 45, 566 (DOI: 10.1103/ PhysRevLett.45.566)

[45] Perdew J.P., Wang Y. Accurate and Simple Analytic Representation of the Electron-Gas Correlation Energy, Phys. Rev. B, 1992, 45, 13244− 13249 (DOI: 10.1103/PhysRevB.45.13244)

[46] Perdew J.P., Burke K., Ernzerhof M. Generalized Gradient Approximation Made Simple, Phys. Rev. Lett., 1996, 77, 3865−3868. (DOI: 10.1103/PhysRevLett.77.3865)

[47] Perdew, J. P.; Burke, K.; Ernzerhof, M. Generalized Gradient Approximation Made Simple [Phys. Rev. Lett. 77, 3865 (1996)]. Phys. Rev. Lett. 1997, 78, 1396 (DOI: 10.1103/PhysRevLett.78.1396

[48] Perdew J.P., Ruzsinszky A., Csonka G.I., Vydrov O.A., Scuseria G.E., Constantin L.A., Zhou X., Burke K. (2008), Restoring the Density-Gradient Expansion for Exchange in Solids and Surfaces, Phys. Rev. Lett., 100, 136406 (DOI: 10.1103/PhysRevLett.100.136406)

[49] Vanderbilt D. Soft Self-Consistent Pseudopotentials in a Generalized Eigenvalue Formalism, Phys. Rev. B, 1990, 41, 7892−7895 (DOI: 10.1103/PhysRevB.41.7892)

[50] Andersen, O.K. Linear Methods in Band Theory, Phys. Rev. B, 1975, 12, 3060−3083 (DOI: 10.1103/PhysRevB.12.3060)

[51] Blochl P.E. Projector Augmented-Wave Method, Phy. Rev. B, 1994, 50, 17953 (DOI: 10.1103/PhysRevB.50.17953)

[52] Hamann D.R., Schlüter M., Chiang C. Norm-Conserving Pseudopotentials, Phys. Rev. Lett., 1979, 43, 1494−1497 (DOI: 10.1103/PhysRevLett.43.1494)

[53] Mortensen, J. J.; Hansen, L. B.; Jacobsen, K. W. Real-Space Grid Implementation of the Projector Augmented Wave Method. Phys. Rev. B: Condens. Matter Mater. Phys. 2005, 71, 035109 (DOI: 10.1103/PhysRevB.71.035109)

[54] Enkovaara, J.; Rostgaard, C.; Mortensen, J. J.; Chen, J.; Dułak, M.; Ferrighi, L.; Gavnholt, J.; Glinsvad, C.; Haikola, V.; Hansen, H. A.; Kristoffersen, H. H.; Kuisma, M.; Larsen, A. H.; Lehtovaara, L.; Ljungberg, M.; Lopez-Acevedo, O.; Moses, P. G.; Ojanen, J.; Olsen, T.; Petzold, V.; Romero, N. A.; Stausholm-Møller, J.; Strange, M.; Tritsaris, G. A.; Vanin, M.; Walter, M.; Hammer, B.; Häkkinen, H.; Madsen, G. K. H.; Nieminen, R. M.; Nørskov, J. K.; Puska, M.; Rantala, T. T.; Schiøtz, J.; Thygesen, K. S.; Jacobsen, K. W. Electronic Structure Calculations with GPAW: a Real-Space Implementation of the Projector Augmented-Wave Method. J. Phys.: Condens. Matter. 2010, 22, 253202 (DOI: 10.1088/0953-8984/22/25/253202)

[55] Larsen, A. H.; Mortensen, J. J.; Blomqvist, J.; Castelli, I. E.; Christensen, R.; Dułak, M.; Friis, J.; Groves, M. N.; Hammer, B.; Hargus, C.; Hermes, E. D.; Jennings, P. C.; Jensen, P. B.; Kermode, J.; Kitchin, J. R.; Kolsbjerg, E. L.; Kubal, J.; Kaasbjerg, K.; Lysgaard, S.; Maronsson, J. B.; Maxson, T.; Olsen, T.; Pastewka, L.; Peterson, A.; Rostgaard, C.; Schiøtz, J.; Schütt, O.; Strange, M.; Thygesen, K. S.; Vegge, T.; Vilhelmsen, L.; Walter, M.; Zeng, Z.; Jacobsen, K. W. The Atomic Simulation Environment-A Python Library for Working

with Atoms. J. Phys.: Condens. Matter. 2017, 29, 273002 (DOI: 10.1088/1361-648X/aa680e)

[56] Denton, A. R.; Ashcroft, N. W. Vegard's law. Phys. Rev. A: At., Mol., Opt. Phys. 1991, 43, 3161−3164 (DOI: 10.1103/PhysRevA.43.3161)

[57] Nørskov, J. K.; Rossmeisl, J.; Logadottir, A.; Lindqvist, L.; Kitchin, J. R.; Bligaard, T.; Jónsson, H. Origin of the Overpotential for Oxygen Reduction at a Fuel-Cell Cathode. J. Phys. Chem. B 2004, 108, 17886−17892 (DOI: 10.1021/jp047349j)

[58] Hamada, I.; Morikawa, Y. Density-Functional Analysis of Hydrogen on Pt(111): Electric Field, Solvent, and Coverage Effects. J. Phys. Chem. C 2008, 112, 10889–10898 (DOI: 10.1021/jp8028787)

[59] T.T.T. Hanh, Y. Takimoto, O. Sugino, First-Principles Thermodynamic Description of Hydrogen Electroadsorption on the Pt(111) Surface, Surf. Sci. 2014, 625, 104−111 (DOI: 10.1016/j.susc.2014.03.006)

[60] Yang, H.; Whitten, J. L. Dissociative Adsorption of H_2 on Ni(111). J. Chem. Phys. 1993, 98, 5039–5049 (DOI: 10.1063/1.464958)

[61] Arboleda, N. B.; Kasai, H.; Dino, W. A.; Nakanishi, H. Potential Energy of H_2 Dissociation and Adsorption on Pt(111) Surface: First-Principles Calculation. Jpn. J. Appl. Phys. 2007, 46, 4233 (DOI: 10.1143/JJAP.46.4233)

[62] Yu, C.; Wang, F.; Zhang, Y.; Zhao, L.; Teng, B.; Fan, M.; Liu, X. H_2 Thermal Desorption Spectra on Pt(111): A Density Functional Theory and Kinetic Monte Carlo Simulation Study. Catalysts. 2018, 8, 450 (DOI: 10.3390/catal8100450)

[63] Wang, T.; Pan, L.; Zhang, X.; Zou, J.-J. Insights into the Pt (111) Surface Aid in Predicting the Selective Hydrogenation Catalyst. Catalysts. 2020, 10, 1473 (DOI: 10.3390/catal10121473)

[64] Schumacher, N.; Boisen, A.; Dahl, S.; Gokhale, A.; Kandoi, S.; Grabow, L.; Dumesic, J.; Mavrikakis, M.; Chorkendorff, I. Trends in Low-Temperature Water-gas Shift Reactivity on Transition

Metals J. Catal. 2005, 229, 265–275 (DOI: 10.1016/j.jcat.2004.10.025)

[65] Callaghan, C. A.; Vilekar, S. A.; Fishtik, I.; Datta, R. Topological Analysis of Catalytic Reaction Networks: Water Gas Shift Reaction on Cu(111). Appl. Catal. A, 2008, 345, 213–232 (DOI: 10.1016/j.apcata.2008.05.004)

[66] Das, A; Mandal, S. C; Nair, A. S; Pathak, B. Computational Screening of First-Row Transition-Metal Based Alloy Catalysts-Ligand Induced N_2 Reduction Reaction Selectivity. ACS Phys. Chem. Au 2022, 2, 2, 125–135 (DOI: 10.1021/acsphyschemau.1c00021)

[67] Thomas, S; Yazdanparas, S; Hildreth, O; Zaeem, M. A. Formation Energies, Electronic Properties and Elemental Diffusion of Cu–Cr–Nb (GRCop) Alloys Phys. B: Condens. Matter 2022, 637, 413909 (DOI: 10.1016/j.physb.2022.413909)

[68] Chen, W; Ding, X; Feng, Y; Liu, X; Liu, K; Lu, Z. P; Li, D; Li, Y; Liu, C. T; Chen X. Q. Vacancy Formation Enthalpies of High-Entropy FeCoCrNi Alloy via First-Principles Calculations and Possible Implications to its Superior Radiation Tolerance. J. Mater. Sci. Technol. 2018, 34, 355–364 (DOI: 10.1016/j.jmst.2017.11.005)

[69] Anasori, B.; Xie, Y.; Beidaghi, M.; Lu, J.; Hosler, B. C.; Hultman, L.; Kent, P. R. C.; Gogotsi, Y.; Barsoum, M. W. Two-Dimensional, Ordered, Double Transition Metals Carbides (MXenes). ACS Nano 2015, 9 (10), 9507–9516 (DOI: 10.1021/acsnano.5b03591)

[70] Guesmi, H. Theoretical Insights on the Effect of Reactive Gas on the Chemical Ordering of Gold-Based Alloys. Gold Bull 2013, 46, 213–219 (DOI: 10.1007/s13404-013-0106-9)

[71] Ma, Y.-Y.; Lang, Z.-L.; Yan, L.-K.; Wang, Y.-H.; Tan, H.-Q.; Feng, K.; Xia, Y.-J.; Zhong, J.; Liu, Y.; Kang, Z.-H.; Li, Y.-G. Highly Efficient Hydrogen Evolution Triggered by a Multi-Interfacial Ni/WC Hybrid Electrocatalyst. Energy Environ. Sci. 2018, 11, 2114–2123 (DOI: 10.1039/C8EE01129J)